Compositive role of refractory element Mo in improving strength and ductility of face-centered-cubic complex concentrated alloys

Jang, Tae Jin; Lee, You Na; Ikeda, Yuji; Körmann, Fritz; Baek, Ju Hyun; Do, Hyeon Seok; Choi, Yeon Taek; Gwon, Hojun; Suh, Jin Yoo; Kim, Hyoung Seop

Important note
To cite this publication, please use the final published version (if applicable).
Please check the document version above.

Full length article

Compositive role of refractory element Mo in improving strength and ductility of face-centered-cubic complex concentrated alloys

Tae Jin Jang [a],[1], You Na Lee [a],[1], Yuji Ikeda [b],[c], Fritz Körmann [c],[d], Ju-Hyun Baek [e], Hyeon-Seok Do [f], Yeon Taek Choi [f], Hojun Gwon [g], Jin-Yoo Suh [e], Hyoung Seop Kim [g],[h], Byeong-Joo Lee [f],[h], Alireza Zargaran [g],[*], Seok Su Sohn [a],[*]

[a] Department of Materials Science and Engineering, Korea University, Seoul 02841, South Korea
[b] Institute for Materials Science, University of Stuttgart, Pfaffenwaldring 55, Stuttgart 70569, Germany
[c] Computational Materials Design, Max–Planck–Institut für Eisenforschung GmbH, Max–Planck–Straße 1, Düsseldorf 40237, Germany
[d] Department of Materials Science and Engineering, Delft University of Technology, Mekelweg 2, Delft 2628 CD, the Netherlands
[e] Energy Materials Research Center, Korea Institute of Science and Technology, Seoul 02792, South Korea
[f] Department of Materials Science and Engineering, Pohang University of Science and Technology, Pohang 37673, South Korea
[g] Graduate Institute of Ferrous Technology, Pohang University of Science and Technology, Pohang 37673, South Korea
[h] Center for Heterogenic Metal Additive Manufacturing, Pohang University of Science and Technology, Pohang 37673, South Korea

ARTICLE INFO

ABSTRACT

Complex concentrated alloys (CCAs) with a face-centered-cubic (FCC) structure exhibit remarkable mechanical properties, introducing the expansion of compositional space in alloy design for structural materials. The formation of a single solid-solution phase is enabled by configuring various 3d-transition elements, while doping other elements even of a small portion generally leads to the formation of brittle intermetallic compounds. Herein, we demonstrate through a systematic investigation of single FCC $(CoNi)_{100-x}Mo_x$ alloys that a wide range of refractory element Mo can simultaneously improve the strength and ductility while sustaining the solid-solution structure. The addition of Mo with a larger atomic size than those of 3d-transition elements introduces severe lattice distortion in the FCC lattice and causes grain-boundary segregation enriched by Mo atoms. In addition, increasing Mo content effectively reduces the stacking fault energy (SFE). The increased lattice distortion with Mo content enhances the solid-solution strengthening of the alloys. Besides, along with reduced SFE and stabilization of the dislocation emission site by grain-boundary segregation, this elevated solid-solution strengthening increases grain-boundary strengthening, reaching a yield strength of ~1 GPa. Moreover, the reduction of SFE with increasing Mo results in the transition of dislocation substructures and the refinement of deformation twins, allowing for enhanced strain-hardening capability and thus ~1.3 GPa tensile strength and ~50% ductility. Such compositive and synergetic effects of refractory element Mo enable the CCAs with a single FCC solid solution to overcome the strength and ductility trade-off.

1. Introduction

CCAs consisting of multiprincipal elements have garnered much attention as a new alloy design strategy over the last two decades owing to the potential for remarkable mechanical properties arising from the numerous combinations of alloying systems, in contrast to conventional dilute alloys [1–4]. In this field, the most widely investigated alloys have a single FCC solid-solution phase represented by CrMnFeCoNi [5], CrFeCoNi [6], CrCoNi [7], and VCoNi [8]. Since the contribution of solid-solution strengthening in dilute FCC alloys is less significant when compared to other strengthening mechanisms, it is generally considered that achieving a high yield strength in single FCC structured alloys is challenging without integrating a high density of defects such as dislocations or precipitates. Against this notion, however, FCC structured CCAs (FCC CCAs) exhibit considerably high yield strength stemming from only two strengthening contributions, that is, solid-solution strengthening and grain-boundary strengthening. In addition, various deformation mechanisms observed in FCC CCAs, e.g., nano–twinning [9,

10], transformation-induced plasticity [11,12], and slip band refinement [13], contribute to a high strain-hardening capacity and consequently an improved uniform ductility.

Owing to the distinctive properties of FCC CCAs, many studies have focused on the requirements for the formation of FCC solid solutions. In this regard, empirical criteria based on the Hume–Rothery rule and thermodynamic parameters are widely accepted for predicting the crystal structure and formation of solid-solution, intermetallic, or amorphous phases [14–16]. For the predicted FCC CCAs, significant efforts have been made to reveal the fundamental mechanisms behind the enhanced solid-solution strengthening and grain-boundary strengthening. Severe lattice distortion facilitates large solid-solution strengthening, where the dominant factors known to control lattice distortion are the average atomic size misfit [17], root-mean-square of atomic displacements [18], charge transfer, and atomic-level pressure [19,20]. In contrast to solid-solution strengthening, only a few investigations on grain-boundary strengthening in CCAs have been conducted [21,22]. Moreover, most studies on the origins of solid-solution and grain-boundary strengthening have only investigated FCC CCAs composed of 3d-transition metal elements. Although other elements with large atomic size differences, such as Al and Mo were added, they contributed to improving the mechanical properties through the formation of various secondary ordered or intermetallic phases [23–27]. In particular, it was suggested that the utilization of a small amount of Mo is an effective strategy to enhance the strength-ductility combination of FCC CCAs by regulating the precipitation behaviors [28,29] or deformation mechanisms. [29,30]. However, the addition of Mo to FCC CCAs generally leads to the formation of topologically close-packed phases with complex crystal structures such as μ [31] and σ phases [32], causing severe embrittlement. He et al. [32] reported that the addition of a small amount of 4 at% Mo in the equiatomic CrCoNi forms the σ phase. In addition, Liu et al. [25] investigated precipitation-hardened CrFeCoNiMo$_{0.3}$ alloys, where up to 6.6 at% Mo is dissolved in the FCC matrix and the remaining Mo forms σ and μ phases. In other words, single-phase FCC CCAs with a wide range of Mo contents have never been experimentally investigated to the best of our knowledge; thus, a systematic investigation on the effect of Mo on solid-solution strengthening, grain-boundary strengthening, and deformation mechanisms in multiprincipal FCC solid-solution alloys is lacking yet.

This study aims to reveal the compositive role of Mo on microstructural evolutions and strengthening mechanisms in single-phase FCC CCAs. Based on thermodynamic calculations, the three alloys with different Mo contents (8, 15, and 18 at%) in a (CoNi)$_{100-x}$Mo$_x$ system were selected as model alloys as it is predicted to have a wide single FCC phase region even with a Mo content as high as 18 at%. To avoid the formation of other phases, such as disordered hexagonal close-packed (HCP) and ordered μ phases, the regions of a single FCC solid solution in these alloys were experimentally confirmed under various annealing conditions. Subsequently, solid-solution and grain-boundary strengthening were quantified on fully FCC-structured specimens across a set of different grain sizes. Our results show that both the strength and ductility improve simultaneously with increasing Mo content. Particularly, the (CoNi)$_{82}$Mo$_{18}$ alloy exhibited an ultrahigh yield strength of ~1 GPa, a tensile strength of ~1.3 GPa, and ductility of ~50% despite being fully recrystallized, i.e., a meager contribution of dislocation density. The underlying effect of Mo on solid-solution strengthening was revealed through correlations between solid-solution strengthening and lattice distortion, computed via *ab initio* calculations. Interestingly, significant grain-boundary strengthening is achieved by increasing the Mo content, which is correlated to the solid-solution strengthening, grain-boundary segregation of Mo, and variations in SFE quantified through *ab initio* calculations and experimental measurements. In addition to the strengthening contributions, the transition of the deformation structure according to SFE contributes to a high strain-hardening rate, and consequently high tensile strength and uniform ductility. This work suggests that the strategy of employing Mo has the

potential to improve the mechanical properties of CCAs to a greater extent.

2. Methodology

2.1. Alloy fabrications

Alloys with nominal compositions of (CoNi)$_{92}$Mo$_8$, (CoNi)$_{85}$Mo$_{15}$, and (CoNi)$_{82}$Mo$_{18}$ (referred to as Mo8, Mo15, and Mo18, respectively) were cast in dimensions of $100{\times}35{\times}8$ mm^3 via vacuum induction melting (MC100V, Indutherm, Germany) using high–purity elements (>99.9%) under Ar atmosphere. The combustion element analysis was performed on the cast ingots using LECO CS230 (LECO, USA) and ELTRA OHN 2000 (ELTRA GmbH, Germany) to measure the content of impurities as listed in Table 1. The cast ingots were homogenized at 1200°C for 2 h under Ar atmosphere, followed by water-quenching, and then cold-rolled to 1.5 mm-thick sheets (~80% reduction in thickness). To obtain fully recrystallized states with various grain sizes, the cold-rolled sheets were annealed at 700–1250°C for 1–60 min under Ar atmosphere, followed by water-quenching to room temperature. For the Mo18 alloy, the above conventional process produces a limited grain size of 4.44

$\pm$2.24 μm at the lowest, which restricts detailed investigations of mechanical behaviors and comparisons with other alloys. Thus, high-pressure torsion (HPT) was conducted on 10 mm-diameter disc specimens with 1.5 mm thickness to enable further grain refinement. Ten turns were performed at 1 rpm under 6 GPa to introduce significant plastic strain, and the specimen was annealed at 1100°C for 1 min followed by water-quenching.

2.2. Microstructural characterizations

The metallographic specimens were prepared by grinding using 320, 400, 600, and 750 grit SiC papers, followed by mechanical polishing with a 1 μm diamond suspension and colloidal silica suspension for 0.5 h to remove the damaged layer on the surface. X-ray diffraction (XRD) analyses (Cu K$_{\alpha1}$ and Cu K$_{\alpha2}$ radiations, scan rate: 5° min^{-1}, scan step size: 0.02°) were performed to identify crystal structures and measure lattice parameters. The weighted average of Cu K$_{\alpha1}$ and Cu K$_{\alpha2}$ radiations were used to measure the lattice parameter. The morphology, size, and distribution of each constituent phase were investigated via field emission scanning electron microscopy (FE-SEM, Quanta FEG 250, FEI, USA) equipped with backscattered electron (BSE) and energy dispersive X-ray (EDS) detectors. Electron backscatter diffraction (EBSD, Digiview, EDAX, USA) was conducted to measure the average grain size of specimens composed of a single FCC phase. The EBSD data were analyzed using TSL-OIM software.

Elemental distribution and grain-boundary segregation analyses were conducted via atom probe tomography (APT, LEAP 4000X HR, Cameca, USA) by applying the pulsed laser mode with a pulse frequency of 200 kHz, energy of 120 pJ at a base temperature of ~50 K, and pressure of ~10^{-11} torr. APT specimens were acquired using a conventional lift-out technique using a focused ion beam (FIB, Ethos NX5000, Hitachi, Japan). APT data were analyzed using the IVAS software provided by Cameca.

Detailed investigations of the phases and deformation structures were conducted using transmission electron microscopy (TEM, JEM-

Table 1
The content of impurities elements of the as-cast (CoNi)$_{100-x}$Mo$_x$ alloys. The content of nitrogen was below the detection limit for all specimens.

Specimen	C (ppm)	S (ppm)	O (ppm)	N
(CoNi)$_{92}$Mo$_8$	45	18	105	-
(CoNi)$_{85}$Mo$_{15}$	37	16	143	-
(CoNi)$_{82}$Mo$_{18}$	37	13	213	-

2100F, JEOL, Japan) operated at a 200 kV voltage equipped with an EDS detector. The TEM specimens were ground to 70 μm and then punched into 3 mm diameter disks. The thin foils were electro-polished using a twin-jet polisher (Tenupol-5, Struers, Denmark) in a solution of 10% perchloric acid and 90% acetic acid at a voltage of 40 V. SFE was measured via weak beam dark-field (DF) TEM analysis using the g(3g) configuration observed from $<111>_{FCC}$ zone axis for the 2% strained tensile specimens. The Burgers vector of the dislocations was determined via g·b analysis using three independent $<2\bar{2}0>$-type diffraction vectors (g = $(02\bar{2})$, g = $(2\bar{2}0)$, and g = $(20\bar{2})$, respectively). The interspacing between the two dissociated Shockley partial dislocations was then measured in the weak beam DF image acquired from the diffraction vector g = $(20\bar{2})$. From the correction method proposed by Cockayne [33], the observed dissociation width of partial dislocations (d_{obs}) was corrected to confirm the actual dissociation width of the partials (d_{act}). SFE values were calculated using the following equation [9,34]:

$$SFE = \frac{Gb_p^2}{8\pi d_{act}}\left(\frac{2-\nu}{1-\nu}\right)\left(1 - \frac{2\nu\cos(2\beta)}{2-\nu}\right) \tag{1}$$

where G is the shear modulus, b_p is the magnitude of the Burgers vectors of partial dislocations, ν is Poisson's ratio, and β is the angle between the dislocation line and the Burgers vector of perfect dislocations.

2.3. Mechanical tests

The elastic properties, *i.e.*, the elastic modulus E, shear modulus G, and Poisson's ratio ν, were measured using a resonant frequency damping analyzer (IMCE RFDA LTVP800) operated in the flexural vibration mode. The specimens for the internal friction tests were prepared with dimensions of 80×20×1.5 mm^2 for the length, width, and thickness, respectively. The E and G moduli were calculated for the flexural vibration mode using the following equations according to ASTM E1876-09 standards.

$$E = 0.9465\left(\frac{mf_r^2}{b}\right)\left(\frac{L^3}{t^3}\right)T \tag{2} \quad G = \frac{4Lm\cdot f_t^2}{bt}\left(\frac{\frac{b}{t}+\frac{t}{b}}{4\left(\frac{t}{b}\right)-2.52\left(\frac{t}{b}\right)^2+0.21\left(\frac{t}{b}\right)^6}\right) \tag{3}$$

where m is the mass of the specimen, b is the width of the specimen, L is the length of the specimen, t is the thickness of the specimen, f_r is the flexural resonant frequency, and T is a correction factor for the fundamental flexural mode that accounts for the finite thickness of the bar. According to the calculated values of E and G, Poisson's ratio ν was acquired from the relationship between E and G, as shown in the following equation:

$$G = \frac{E}{2(1+\nu)} \tag{4}$$

To evaluate the tensile properties, dog-bone-shaped flat tensile specimens with gauge lengths, widths, and thicknesses of 12, 4, and 1.5 mm, respectively, were prepared from the annealed sheets. In the case of the HPT-processed specimens, dog-bone-shaped tensile specimens with a gauge length, width, and thickness of 1.5 mm, 0.7 mm, and 0.8 mm, respectively, were prepared. Uniaxial tensile tests were performed using a universal testing machine (model 3367, Instron, USA) at a strain rate of 10^{-3} s^{-1} at room temperature. The tensile strain was measured using a digital image correlation (DIC) technique with a 3D optical deformation analysis system (ARAMIS 12M, GOM, Germany).

2.4. Ab initio calculation

FCC (CoNi)$_{100-x}$Mo$_x$ alloys with x = 0, 5, 10, 15, and 20 at% were modeled using 120-atom supercells. The supercell models contain six {111} planes along the z-axis. Each plane accommodates 20 atoms and has dimensions of $5a \times 2\sqrt{3}a$, where a is the FCC lattice parameter. The chemical disorder was modeled using special quasirandom structure (SQS) configurations [35]. The correlation functions of the first, second, and third nearest-neighbor doublet clusters as well as the first nearest-neighbor triplet and quartet clusters were optimized to be close to the ideal values of fully random configurations using the simulated annealing approach, as implemented in the ICET code [36].

The SFEs were computed using the tilted supercell approach [37,38]. An intrinsic stacking fault (SF) was created in the perfect FCC cell by tilting the lattice vector along the $\langle 111 \rangle$ direction by $\langle 11\bar{2} \rangle/3$. Thus, the $\cdots$ABCABC$\cdots$ stacking of the {111} planes of the perfect FCC phase is modified to $\cdots$ABC|BCA$\cdots$, where the vertical line indicates the position of the SF. The SF can be introduced at any interlayer space of the {111} planes; therefore, in our six-layer models, six possible SF positions exist. Further, for each SF position, three possible tilting directions exist as $\langle \bar{2}11 \rangle$, $\langle 1\bar{2}1 \rangle$, and $\langle 11\bar{2} \rangle$. Therefore, 18 possible configurations containing SF for the constructed SQS supercells are considered, which could in principle provide different energies owing to the different realizations of chemical randomness in the vicinity of the SF. Depending on the utilized supercell size, this could result in substantial fluctuations in the computed SFEs depending on the local chemical environment near the SF [39,40]. To average out this impact, all 18 configurations were computed for each composition in this study. From the resulting supercell models with and without SFs, the SFE was computed as

$$SFE = \frac{F^{FCC+SF} - F^{FCC}}{A}, \tag{5}$$

where F^{FCC+SF} and F^{FCC} are the Helmholtz energies of the supercell models with and without SFs, respectively, and A denotes the area of the SFs.

Ab initio density functional theory calculations were performed using the VASP code [41–43] with the plane-wave projector augmented wave (PAW) method [44]. The exchange-correlation energy was obtained within the generalized gradient approximation (GGA) of the Perdew–Burke–Ernzerhof (PBE) form [45]. The plane-wave cut-off energy was set to 400 eV. Reciprocal spaces were sampled using a Γ-centered 3×5×3 k-point mesh for the 120-atom models, and the Methfessel–Paxton method [46] with a smearing width of 0.1 eV was applied. The 3d4s orbitals of Co and Ni and the 4d5s orbitals of Mo were treated as the valence states. The total energies were minimized until they converged to within 5×10^{-4} eV per simulation cell for each ionic step. All calculations were performed considering the spin polarization.

The calculations were performed for six volumes around the equilibrium ones. The atoms were initially placed on the ideal close-packing positions and then relaxed by fixing the cell shape until all forces on the atoms converged within 5×10^{-2} eV/A. For each composition, the equilibrium volume and energy were obtained by fitting the obtained energy–volume relation to the Vinet equation of state [47,48]. For the models with SFs, all 18 configurations were employed to obtain a fitted energy–volume curve for each composition. The impact of lattice vibrations on the Helmholtz energies in Eq. (5) was evaluated based on the Debye–Grüneisen model [49]. The Helmholtz energies were evaluated at the equilibrium volumes derived from the fitted energy–volume curves and the thus obtained lattice vibrational contributions. Since the present alloys are ferromagnetic at room temperature, entropic effect of magnetic fluctuations on the SFE is expected to be negligible and hence not considered.

In previous studies [8,13,18], *ab initio* computed root-mean-square (RMS) atomic displacements showed strong correlations with solid-solution strengthening and can, hence, be expected to be a good descriptor of the solid-solution strengthening of alloys. Therefore, we computed the RMS atomic displacements from the ideal FCC lattice sites to the relaxed atomic positions of the alloy models investigated in this study. In addition, charge transfer among atoms can also correlate well with local lattice distortions [13,20]. Thus, we computed the Bader

atomic charges based on the Yu–Trinkle algorithm [50] as implemented by Henkelman et al. [51–53]. For these quantities, calculations were first performed for each volume, and the values at the *ab initio* equilibrium volume were then estimated by linear interpolation.

3. Results

3.1. Thermodynamic calculations

The Co–Ni binary system can form an FCC solid solution without intermetallic compounds in all composition ranges above 422°C owing to their identical FCC crystal structure and low mixing enthalpy (~0 kJ). This considerably large FCC region enables the CoNi binary alloys to accommodate large amounts of Mo despite its different electronic, structural, and atomic-scale characteristics, which motivated the present study. The effect of Mo on the equilibrium states of the equiatomic CoNi binary system was predicted by the thermodynamic calculation using the TCFE2000 database and its upgraded version [54–56]. Fig. 1 shows the equilibrium pseudo-binary phase diagram of the $(CoNi)_{100-x}Mo_x$ alloy system (x = 0–30 at%) in the temperature range of 0–1600°C. With increasing Mo content, it is predicted that a higher temperature is required to achieve a single FCC phase and that such a single FCC solid solution can be maintained up to ~20 at% of Mo. On the other hand, when the Mo content further increases or the temperature decreases, long-range ordered structures such as μ, MoNi, $MoNi_3$, and Co_3Mo are predicted as equilibrium phases. As well as ordered structures, the phase diagram also predicts the disordered FCC and HCP dual–phase regions at intermediate temperatures. Based on this thermodynamic calculation, three compositions of $(CoNi)_{92}Mo_8$, $(CoNi)_{85}Mo_{15}$, and $(CoNi)_{82}Mo_{18}$ were selected as model alloys, which are expected to have a single FCC solid solution at temperatures highlighted by the dark blue region.

3.2. Microstructural evolutions

The XRD profiles for the Mo8 specimens in Fig. 2a reveal only primary FCC peaks to be present in all specimens annealed from 700°C to 1100°C, as plotted in red lines. On the other hand, secondary HCP peaks were also observed in alloys with higher Mo content (Fig. 2b,c), as

plotted in black lines. The HCP peaks in the Mo15 and Mo18 alloys disappeared at temperatures above 1000°C and 1050°C, respectively, and only the primary FCC peaks remained. Fig. 2d shows the lattice parameters acquired from the specimens with a single FCC structure. The parameters of the Mo8, Mo15, and Mo18 alloys are 3.564, 3.587, and 3.602 Å, respectively, revealing a proportional increase with Mo in the CoNi equiatomic alloy [57].

Consistent with the XRD results, the Mo8, Mo15, and Mo18 specimens annealed at temperatures above 700°C (Fig. 3a₁–a₄), 1000°C (Fig. 3b₁,b₂), and 1050°C (Fig. 3c₁) exhibit a recrystallized FCC structure with annealing twins (highlighted by red-dotted boxes in Fig. 3). The SEM-EDS maps also indicate that these specimens have homogeneous elemental distribution in the single FCC phase without distinct element partitioning (Supplementary Fig. 1). In the case of Mo15 (Fig. 3b₃,b₄) and Mo18 (Fig. 3c₂–c₄), the specimens annealed at lower temperatures exhibit more complex microstructures (highlighted by blue-dashed boxes in Fig. 3). These specimens contain bright particles, indicated by red arrows, distributed mainly at the grain boundaries and triple junctions. The bright particles shown in the BSE images are expected to be enriched by Mo, which has a higher atomic number than that of Co or Ni. Meanwhile, it is expected that the HCP phase, which is predicted through thermodynamic calculations and identified by XRD analyses, is formed inside the grains with the shape of plates parallel to the FCC annealing twins. Interestingly, the Mo18 alloy specimens (Fig. 3c₂–c₄) show fine lamellar structures composed of an FCC matrix, FCC annealing twins, and HCP plates as indicated by blue arrows. The average thickness of these lamellar structures of the Mo18 alloy becomes finer from ~89 nm to ~21 nm as the annealing temperature decreases from 1000°C to 800°C.

Further detailed identification of the phases was performed on the complex microstructures in the specimens corresponding to Fig. 3b₃ and 3c₂ via TEM analysis. Fig. 4a₁–a₄ reveals the lamellar structure of Mo15 specimens annealed at 900°C for 1 h. The selected area diffraction pattern (SADP) and DF images taken along the $<110>_{FCC}$ zone axis show that the lamellar structure is composed of FCC twins and HCP plates in the FCC matrix. The crystallographic orientation relationship between FCC and HCP follows the Shoji–Nishiyama (S–N) relation, that is, $<11\bar{2}0>_{HCP}//<110>_{FCC}$ and $\{0002\}_{HCP}//\{111\}_{FCC}$ [58]. In contrast to the thermodynamic prediction that only disordered HCP and FCC
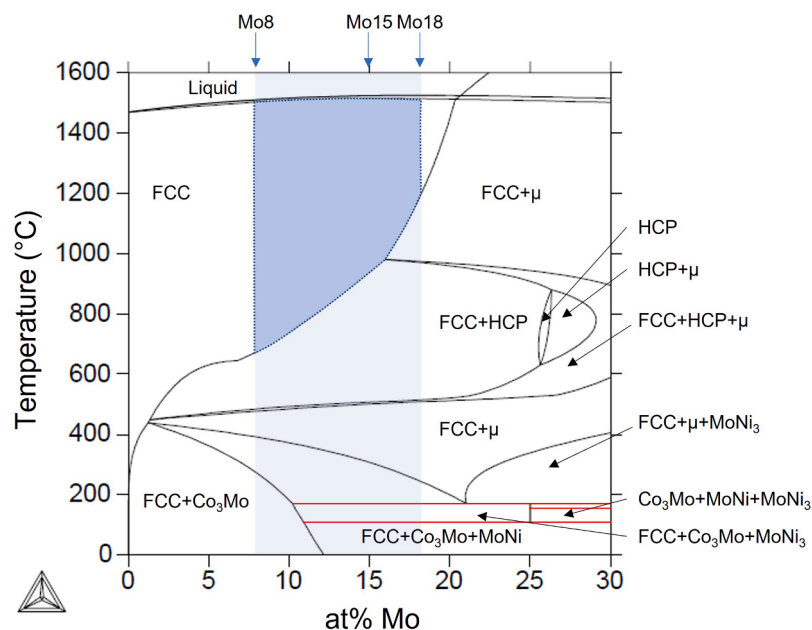

Fig. 1. Equilibrium pseudo-binary phase diagram of the $(CoNi)_{100-x}Mo_x$ alloy system (x = 0–30 at%) in the temperature range of 0–1600°C. The composition range from $(CoNi)_{92}Mo_8$ to $(CoNi)_{82}Mo_{18}$ is highlighted in blue color.
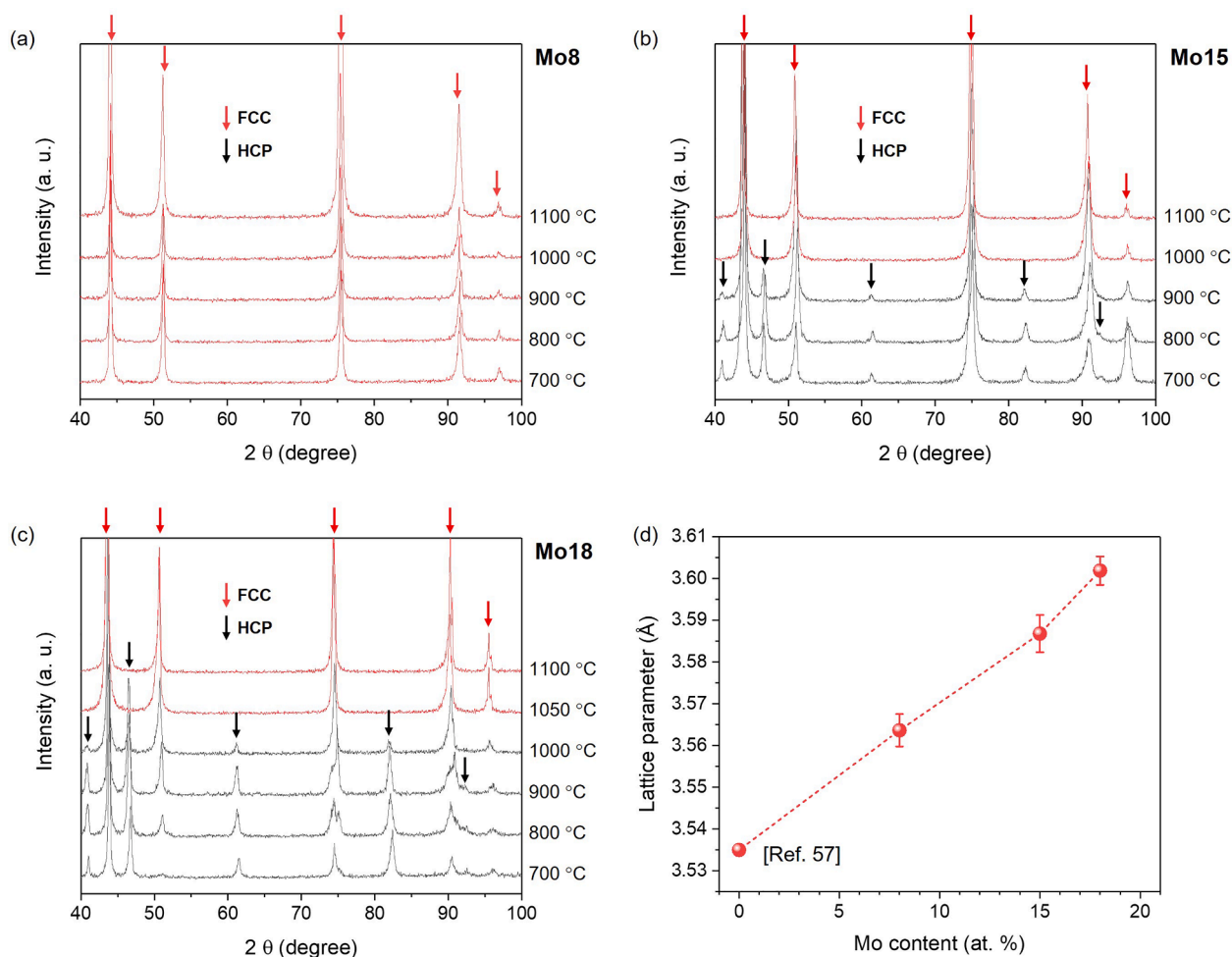
Fig. 2. Phase identification via XRD analysis of the (a) Mo8, (b) Mo15, and (c) Mo18 alloys annealed at different temperatures for 1 h. (d) Calculated lattice parameters of the FCC phase for the present alloys as well as the equiatomic CoNi binary alloy.

phases exist at intermediate temperatures, superlattice peaks corresponding to the Co_3Mo–type $D0_{19}$ structure with a two-layered ordered HCP structure [59], appeared in the SADP as indicated by the red rectangle. The DF image acquired from this superlattice peak (Fig. 4a$_4$) confirms that the disordered HCP plates partially have an ordered $D0_{19}$ structure, resulting in lamellar structures composed of the FCC, HCP, and $D0_{19}$ phases.

The Mo18 specimen annealed at 1000°C for 1 h also presents such lamellar structures consisting of FCC twins, HCP plates, and $D0_{19}$ (Fig. 4b$_1$–b$_4$). Compared to those in Mo15, these lamellar structures have a higher fraction and larger thickness of HCP and $D0_{19}$ plates. The compositional profile across these lamellar structures (Fig. 4c) reveals that the disordered HCP and ordered $D0_{19}$ have an identical Mo-rich composition of 40Co–35Ni–25Mo (at%), whereas the FCC has a composition of 42Co–40Ni–18Mo (at%). The bright particles observed at the triple junction (red arrows in Fig. 3) were also confirmed to have an ordered $D0_{19}$ structure (Fig. 4d) with the same composition as the $D0_{19}$ present in the FCC and HCP plates (Supplementary Fig. 2). Finally, Fig. 4e confirms a single FCC structure with annealing twins and the absence of nanosized precipitates in the Mo18 alloy annealed at 1050°C for 1 h (Fig. 3c$_1$).

To investigate whether the Mo18 alloy with a single FCC phase exhibits elemental heterogeneity, APT analysis was performed on the specimen annealed at 1050°C for 1 h (Fig. 3c$_1$). Fig. 5a shows the FIB-milled tip specimen containing a grain boundary, in which the fast Fourier transformation (FFT) pattern indicates two grains with different crystallographic orientations across the grain boundary. The three-

dimensional reconstruction map (Fig. 5b) reveals that all constituent elements are homogeneously distributed at the grain interiors. The one-dimensional concentration profile acquired across the grain boundary (Fig. 5c) indicates that the matrices exhibit a homogeneous composition of 42Co–39Ni–19Mo (at%), which corresponds well with the nominal composition of the alloy. In addition, the FCC matrices of Mo18 maintain random solid-solution states. However, the grain boundary is considerably decorated with Mo (up to ~32 at%), whereas Co and Ni are depleted in this region. Such grain-boundary segregation of substitutional elements is often observed in other polycrystalline FCC CCAs [8, 60], and the segregation of Mo at the grain boundary can be attributed to the relaxation of the elastic strain field induced by Mo being larger than Co and Ni.

3.3. Mechanical properties of single FCC solid-solution alloys

The grain size plays a critical role in determining the mechanical response of single FCC solid-solution alloys. To investigate the dependency of mechanical properties on the grain size, Mo8, Mo15, and Mo18 alloys were annealed under various time and temperature conditions to obtain a set of single FCC structured specimens with diverse grain sizes. The annealing temperatures were determined based on the critical temperature resulting in a single FCC phase (Figs. 2 and 3): 700–1200°C for Mo8, 1000–1200°C for Mo15, and 1050–1250°C for Mo18. All specimens display a recrystallized FCC structure (Supplementary Fig. 3) with various average grain sizes in the range of ~2–60 μm. As aforementioned, further refinement below 3 μm through
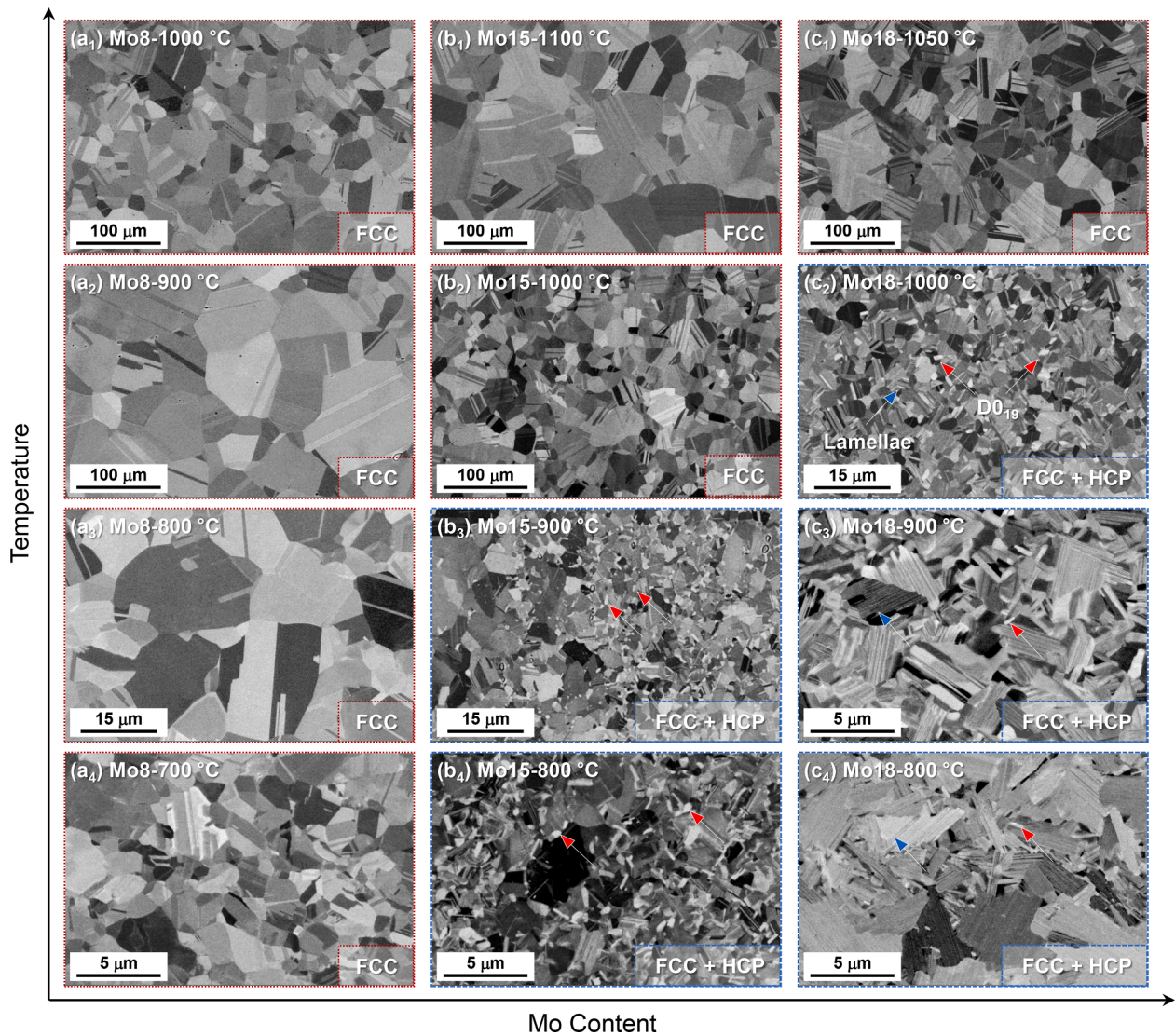
Fig. 3. BSE images of the (a$_1$–a$_4$) Mo8, (b$_1$–b$_4$) Mo15, and (c$_1$–c$_4$) Mo18 alloys annealed at various temperatures for 1 h. The specimens of single FCC solid-solution and FCC-HCP dual phases are outlined as red-dotted and blue-dashed boxes, respectively.

conventional processing is difficult for Mo18 as the single FCC is obtained at a relatively high temperature preventing fine-grained structuring. Thus, HPT imposing abundant nucleation sites for recrystallization was introduced and followed by subsequent short-duration annealing (1 min), resulting in an average grain size of 1.9 μm (Supplementary Fig. 3c$_6$).

The processing conditions, average grain sizes, and mechanical properties are listed in Table 2. Fig. 6a–c presents representative room–temperature engineering stress–strain curves of the single FCC solid-solution alloys with various grain sizes. Mo8, Mo15, and Mo18 annealed at 1200°C for 1 h exhibit yield strength of 244 MPa, 322 MPa, and 382 MPa and ductility of 55.7 %, 69.8 %, and 71.6 %, respectively, confirming both yield strength and ductility improved simultaneously with increasing Mo content. This tendency remains even when the grain size is reduced, indicating that both strength and ductility are the highest in the Mo18 alloy specimens. Notably, the sensitivity of the yield strength to the grain size also increases with increasing Mo content. When the grain size decreases from 4.4 μm to 1.9 μm, the yield strength of the Mo18 alloy significantly increases by 330 MPa. Consequently, this alloy exhibits a very high yield strength of ~1 GPa despite being in the recrystallized state with a single FCC solid solution.

More quantitatively, the dependence of the yield stress on grain sizes can be represented in terms of the Hall–Petch relationship, as expressed by the following equation [61,62]:

$$\sigma_y = \sigma_0 + k_y d^{-1/2}, \tag{6}$$

where σ_0 is solid-solution strengthening, often referred to as lattice friction stress; k_y is the Hall–Petch coefficient indicating the strength sensitivity to grain size changes; and d is the average grain size. Fig. 6d reveals that the relationship between grain size and yield strength for the present alloys agrees well with the Hall–Petch equation, showing an R-square value of ~99 %. Interestingly, as the Mo content increases, both the solid-solution strengthening and the Hall–Petch coefficient increase. Of particular significance is the solid-solution strengthening of 229 MPa and the Hall–Petch coefficient of 1028 MPa·μm$^{1/2}$ in the Mo18 alloy, which is considerably higher than that of previously reported FCC CCAs (Table 3). Such high solid-solution strengthening and Hall–Petch coefficient enable the Mo18 alloy, with a single FCC solid solution and an average grain size of 1.9 μm, to achieve a yield strength of ~1 GPa without other strengthening contributions, such as precipitation strengthening or dislocation strengthening.

In addition to the yield strength, the variation in the strain-hardening capacity according to the Mo content should be noted. Fig. 6e shows the strain-hardening rate curves of the three alloys with a similar grain size
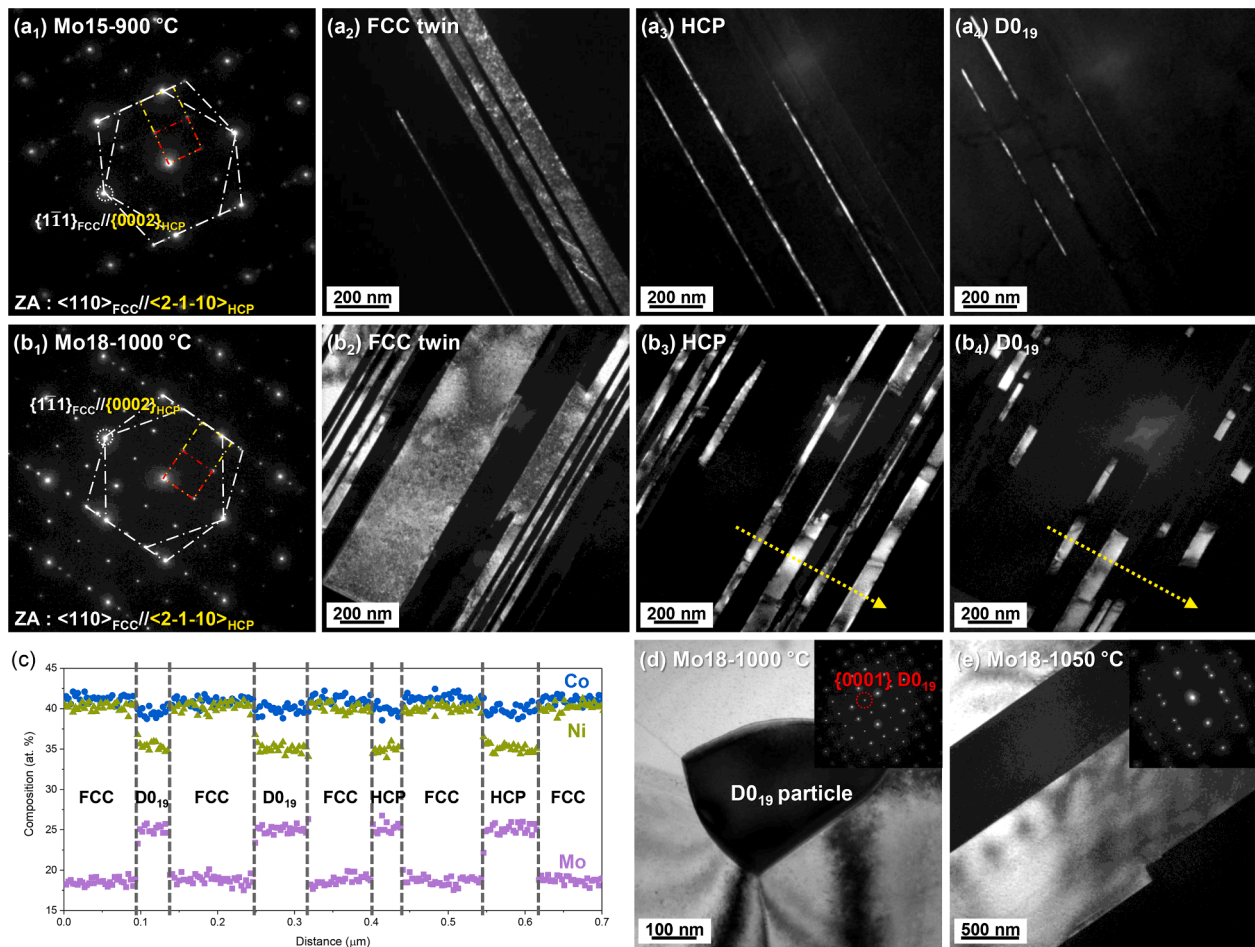
Fig. 4. Phase characterizations via TEM analysis. SADP of the (a_1) Mo15 alloy annealed at 900°C and (b_1) Mo18 alloy annealed at 1000°C. Corresponding DF images for (a_2, b_2) revealing FCC annealing twins, (a_3, b_3) HCP plates, and (a_4, a_4) ordered $D0_{19}$ structure. (c) TEM-EDS line profile along the yellow arrow shown in (b_3) and (b_4). (d) BF image and SADP (inset) of the $D0_{19}$ particle at the triple junction of grains in the Mo18 alloy annealed at 1000°C. (e) DF image showing FCC matrix, annealing twin, and their corresponding SADP (inset) in the Mo18 alloy annealed at 1050°C.
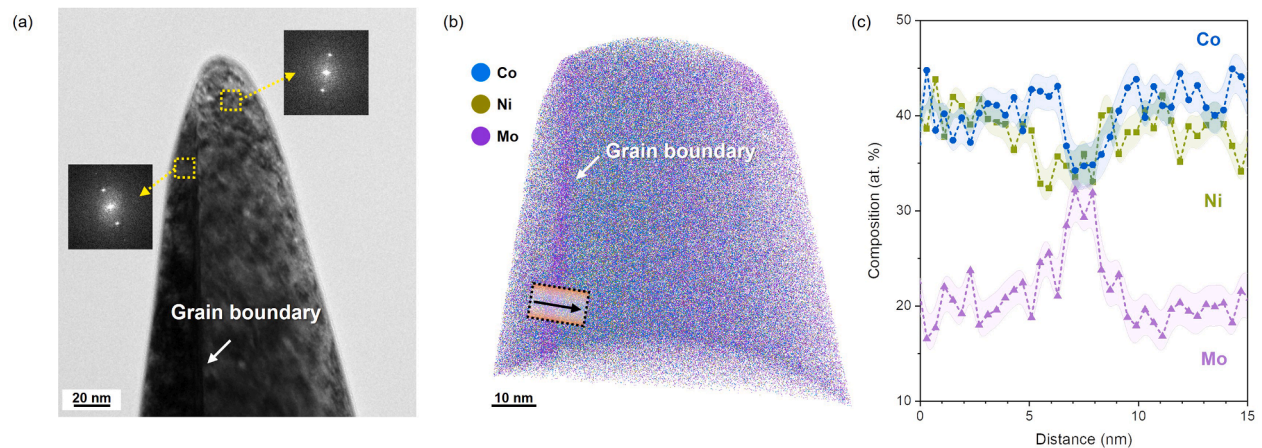
Fig. 5. APT elemental distribution analysis of the Mo18 alloy consisting of a single FCC phase: (a) FIB-milled tip specimen containing a grain boundary. (b) Three-dimensional reconstructions of Co, Ni, and Mo. (c) One-dimensional compositional profile along the black arrow shown in (b).

of ~4 μm. At the initiation of plastic deformation in Mo15 and Mo18, the rapid drop in the strain-hardening rate is considered to result from the lack of sufficient mobile dislocations, as typically reported in materials with grain sizes less than a few micrometers [63]. After the initial plastic strain regime, the strain-hardening rates of all alloys exhibit similar trends, with a rapid decrease until ~8 % true strain, followed by a decelerated decrease until plastic instability. Aside from the shape of strain-hardening rate curves, the strain-hardening rate increases as the Mo content increases. Thus, Mo18 exhibits the highest strain-hardening rate among the three alloys. This high hardening rate delays the onset of plastic instability and contributes to a high tensile ductility. The mechanical properties determined in this study are compared with those of

Table 2
Tensile properties and average grain sizes of the single FCC structured $(CoNi)_{100-x}Mo_x$ alloys at various processing conditions.

Specimen	Processing condition	Average grain size (μm)	Yield strength (MPa)	Tensile strength (MPa)	Total elongation (%)
$(CoNi)_{92}Mo_8$	CR (80%) + 700°C / 1 h	1.98 ± 1.12	686	938	41.5
	CR (80%) + 750°C / 1 h	2.39 ± 1.36	601	896	42.8
	CR (80%) + 800°C / 1 h	4.60 ± 3.24	511	851	44.2
	CR (80%) + 900°C / 1 h	9.34 ± 4.79	372	784	46.4
	CR (80%) + 1000°C / 1 h	22.2 ± 11.5	296	741	55.7
	CR (80%) + 1200°C / 1 h	38.7 ± 20.2	244	708	56.6
$(CoNi)_{85}Mo_{15}$	CR (80%) + 1000°C / 1 m	2.27 ± 1.45	816	1193	42.1
	CR (80%) + 1000°C / 1 m 30 s	3.08 ± 1.65	727	1135	51.3
	CR (80%) + 1000°C / 2 m	3.70 ± 1.90	687	1111	52.1
	CR (80%) + 1000°C / 5 m	7.33 ± 3.49	575	1068	54.1
	CR (80%) + 1000°C / 1 h	18.8 ± 8.78	445	973	56.9
	CR (80%) + 1200°C / 1 h	38.0 ± 21.7	332	908	69.8
$(CoNi)_{82}Mo_{18}$	HPT + 1100°C / 1m	1.85 ± 0.86	1005	1326	51.5
	CR (80%) + 1050°C / 2 m	4.44 ± 2.24	674	1157	52.2
	CR (80%) + 1100°C / 2 m	11.3 ± 5.10	545	1085	56.6
	CR (80%) + 1100°C / 10 m	28.2 ± 14.4	438	1007	70.4
	CR (80%) + 1200°C / 1 h	44.1 ± 22.5	382	963	71.6
	CR (80%) + 1250°C / 1 h	58.2 ± 31.5	363	958	69.2

other conventional steels and CCAs in Fig. 6f, confirming that the strength-ductility trade-off relation can be overcome by Mo addition; thus, the Mo18 alloy can achieve remarkable properties by grain refinement.

3.4. Deformation structures

To unravel underlying deformation mechanisms in $(CoNi)_{100-x}Mo_x$ systems, detailed TEM analysis was performed on the tensile specimens with an average grain size of ~4 μm, deformed to two different strain levels of 2% (Fig. 7) and 30% (Fig. 8), respectively. The scanning TEM (STEM) images at 2% strain (Fig. 7a,c,e) reveal that plastic strain accumulated along several {111} planes of FCC lattice via dislocation slip mechanisms, consistent with previous studies on FCC solid-solution alloys. All specimens show the formation of SFs indicated by red arrows (Fig. 7b,d,f), revealing widely separated Shockley partial dislocations. This result implies that the present $(CoNi)_{100-x}Mo_x$ alloys show deformation structures of the low-SFE regime. In addition, dislocation nodes, which can hamper the subsequent dislocation glide due to their stable configuration [64], are observed with spanning SFs between them. For alloys with low SFE, it is known that an association of partial dislocations necessary for cross-slip is suppressed; thus, the deformation exhibits planar characteristics [65,66]. The planar characteristics of the

dislocation arrangement in the $(CoNi)_{100-x}Mo_x$ alloys become more robust with increasing Mo content. Particularly, in the Mo18 alloy exhibiting a sharp dislocation arrangement along the {111} planes, the SF layers on successive {111} planes, *i.e.*, nano-twin, are also observed in the 2%-strained specimen, as indicated by white arrows in Fig. 7g,h.

Further plastic straining to 30% results in distinct planar characteristics with a high density of dislocations (Fig. 8a–c). In addition to the increment of dislocation density, plastic strain accommodation occurred simultaneously through another deformation mechanism known as deformation twinning. For all specimens, additional diffraction spots corresponding to deformation twins were observed in the SADP obtained from the <110> zone axis. The DF images obtained using these additional {111}-type g vectors (Fig. 8d–f) indicate well-defined twin substructures along the {111} planes. With increasing Mo content, the thickness and the interspacing of the twins reduce, resulting in refined twinning substructures for the Mo15 and Mo18 alloys. In particular, the Mo18 alloy exhibits the highest twinning activity among the present alloys: an average twin thickness of ~8.7 nm and interspacing of ~33.7 nm. In addition to the twin substructure, the dislocation substructure varies with the Mo content. For the Mo8 alloy (Fig. 8a), a high density of dislocations induced by large plastic deformation accumulated in the form of dislocation cells (DCs) inside the grains. Notably, the DCs were penetrated by deformation twins. With increasing Mo content, no prominent DC formation was observed (Fig. 8b,c). Rather, the dislocation substructures were altered from DCs to high-density dislocation walls (HDDWs). Fig. 8c clearly shows the Mo18 alloy with the dislocation substructure of HDDWs penetrated by refined deformation twins.

4. Discussion

4.1. Solid-solution stability and solid-solution strengthening

The Hume–Rothery rules are effective means of determining the formation of solid solutions, which is preferred when the systems consist of elements with similar atomic sizes, crystal structures, electronegativities, and valencies. Because the border between the solvent and solute gradually becomes meaningless when configuring CCAs, empirical criteria for predicting solid-solution phase formation have been developed through extended Hume–Rothery rules and thermodynamic parameters [14,16,67]. According to these criteria, for a single FCC solid-solution, the following composition-weighted terms fulfill these requirements: i) atomic size difference (δ ≤ 6.6%), ii) atomic packing parameter (γ ≤ 1.175), iii) mixing enthalpy (-15 kJ mol^{-1} < ΔH_{mix} < 5 kJ mol^{-1}), and iv) average valence electron concentration (VEC ≥ 8.0). Table 4 reveals that the Mo8, Mo15, and Mo18 alloys satisfy the empirical criteria for the formation of a single FCC solid solution. Compared to previously reported FCC CCAs composed of 3d-transition metals, the $(CoNi)_{100-x}Mo_x$ alloys exhibit higher values of δ and γ, which are associated with the large atomic size difference between refractory elements (Mo) and 3d-transition metal elements (Co, Ni) [68].

The large atomic size difference substantially introduces a decrease in the stability of the solid solution in terms of the lattice strain energy [69]. As illustrated in Figs. 2 and 3, a higher temperature is required to maintain a single FCC solid-solution phase with increasing Mo content, indicating a reduction in structural stability in the FCC solid solution. Below the temperature of the single FCC phase region, where the effect of configurational entropy is reduced while that of enthalpy becomes dominant, Mo15 and Mo18 decompose into disordered FCC and HCP solid solutions, and ordered $D0_{19}$ (Fig. 4). The thermodynamic calculation also demonstrates a reduction in the thermodynamic stability of the FCC solid solution with increasing Mo concentration. The minimum temperature required to form a single FCC solid solution increases from 660 to 1200°C when the Mo content is increased from 8 to 18 at%. Although $D0_{19}$ is not predicted to be an equilibrium phase in the intermediate temperature region, it may be attributed to the partial disorder-order transformation, considering that Co_3Mo having the $D0_{19}$
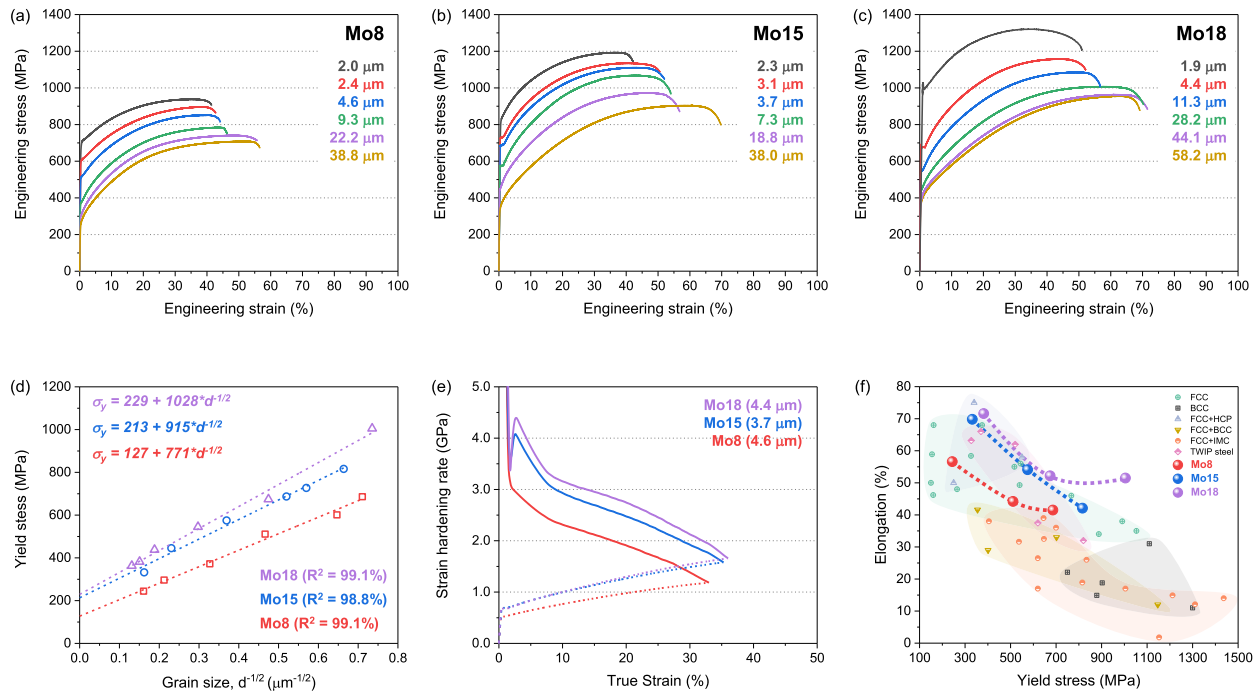
Fig. 6. Mechanical properties of the $(CoNi)_{100-x}Mo_x$ alloys. Engineering tensile stress–strain curves at room temperature of the (a) Mo8, (b) Mo15, and (c) Mo18 alloys. (d) Yield stress (measured by 0.2% offset) versus the reciprocal of the square root of the average grain size of the alloys. (e) Strain-hardening rate curves of the annealed alloys with similar grain sizes. (f) Overview of the yield strength versus tensile elongation compared to other CCAs and TWIP steels. Detailed compositions and properties of the CCAs and TWIP steel are summarized in Supplementary Table 1.

Table 3

Shear modulus (G), Poisson's ratio (ν), solid-solution strengthening (σ_0), and Hall–Petch coefficient (k_y) of the various FCC CCAs, CoNi binary alloy, and pure Ni.

	G (GPa)	ν	σ_0 (MPa)	k_y (MPa·μm$^{1/2}$)	Refs.
Ni	76	0.31	22	180	[4,17]
Ni-40Co	86	0.29	52	181	[4,17]
FeCoNi	60	0.35	63	366	[4,17]
CrCoNi	87	0.30	216	568	[4,10,17]
$V_{0.4}Cr_{0.6}CoNi$	85	0.31	296	755	[13]
$V_{0.7}Cr_{0.3}CoNi$	90	0.31	337	844	[13]
VCoNi	72	0.33	380	878	[8]
CrFeCoNi	84	0.28	123	276	[4,17]
CrFeMnCoNi	80	0.26	125	494	[4,17]
$(CoNi)_{92}Mo_8$	85	0.31	127	771	This work
$(CoNi)_{85}Mo_{15}$	98	0.29	213	915	This work
$(CoNi)_{82}Mo_{18}$	96	0.32	229	1028	This work

structure is stable at low temperatures and that both have identical compositions (Fig. 4c).

The addition of Mo to the equiatomic binary CoNi alloy not only affects the solid-solution stability but also improves the solid-solution strengthening from 59 MPa in the CoNi alloy [70] to 229 MPa in the Mo18 alloy. Solid-solution strengthening in CCAs is generally attributed to their distorted lattice and the subsequent local fluctuation in the solute-dislocation interaction energy [19,71]. To describe the lattice distortion and solid-solution strengthening of CCAs with various elemental combinations, new approaches have been proposed beyond the solid-solution strengthening model based on the classical solvent–solute concept used in conventional alloys. Oh et al. [19,20] demonstrated that the atomic-level pressure, which originates from charge transfer among the constituent elements, introduces a local fluctuation in the elastic strain field in the lattice and thus lattice distortion. Okamoto et al. [18] reported that the RMS atomic displacement, which indicates how far each element deviates from its ideal

lattice site on average, can represent lattice distortion and correlate well with the solid-solution strengthening of CCAs. To verify that these approaches can also be applied to the $(CoNi)_{100-x}Mo_x$ system containing the refractory element Mo, *ab initio* calculations were performed as follows.

First, for the calculation of atomic charge transfer, the relationship between the Bader volume and the Bader charge (charge transfer) for each element at each alloy composition and volume was computed based on Bader analysis (Supplementary Fig. 4). Mo atoms are found to have positive Bader charges, whereas those of Ni and Co atoms are distributed around zero, and the overall Bader charge differences are found to increase with increasing Mo content. For each alloy and constituent element, the Bader volumes and charges are negatively correlated. The same trend is also observed for various other FCC [20] and BCC [72] CCAs. Fig. 9a summarizes the standard deviation (SD) of the Bader charge, displaying that the overall scattering in the charge transfer of the constituent elements increases with increasing Mo content. It has been reported that a large scattering in charge transfer introduces a higher atomic level pressure [19], which suggests a greater lattice distortion in alloys with higher Mo content.

In addition to the charge transfer effect, the RMS atomic displacement of the $(CoNi)_{100-x}Mo_x$ system was also computed from the ideal FCC lattice sites to the relaxed atomic positions with equilibrium volumes (see Supplementary Note 1). As shown in Fig. 9b, similar to charge transfer, the overall RMS atomic displacement increases significantly with increasing Mo content. When the concentration of Mo exceeds 10 at %, the Mo atoms show the largest RMS atomic displacements, followed by Co and Ni. This may be the consequence of Mo having a substantially larger atomic volume than Co and Ni; unless in a dilute concentration where Mo atoms are mostly surrounded by Co and Ni, Mo atoms repel each other from ideal FCC lattice sites. Note that the RMS atomic displacement may be affected by chemical short-range order, as previously demonstrated for the VCoNi alloy [73]. A comparison of the RMS atomic displacement in the $(CoNi)_{100-x}Mo_x$ system with other FCC CCAs (Fig. 9c) reveals that even small additions of Mo can considerably

Fig. 7. Deformation structures of the Mo8, Mo15, and Mo18 alloys, with similar grain sizes, deformed to an engineering strain of 2%. STEM images of the (a, b) Mo8, (c, d) Mo15, and (e, f) Mo18 alloys. (g) High-resolution TEM image and (h) FFT pattern obtained from the Mo18 alloy showing the additional diffraction spots corresponding to the nano-twins.
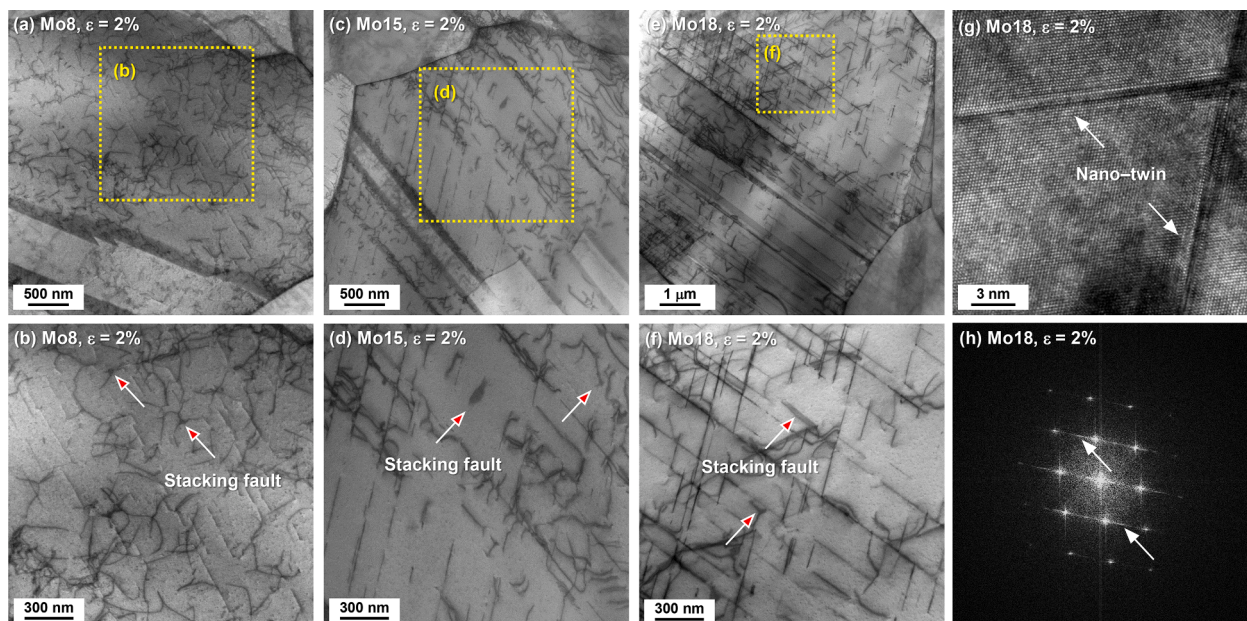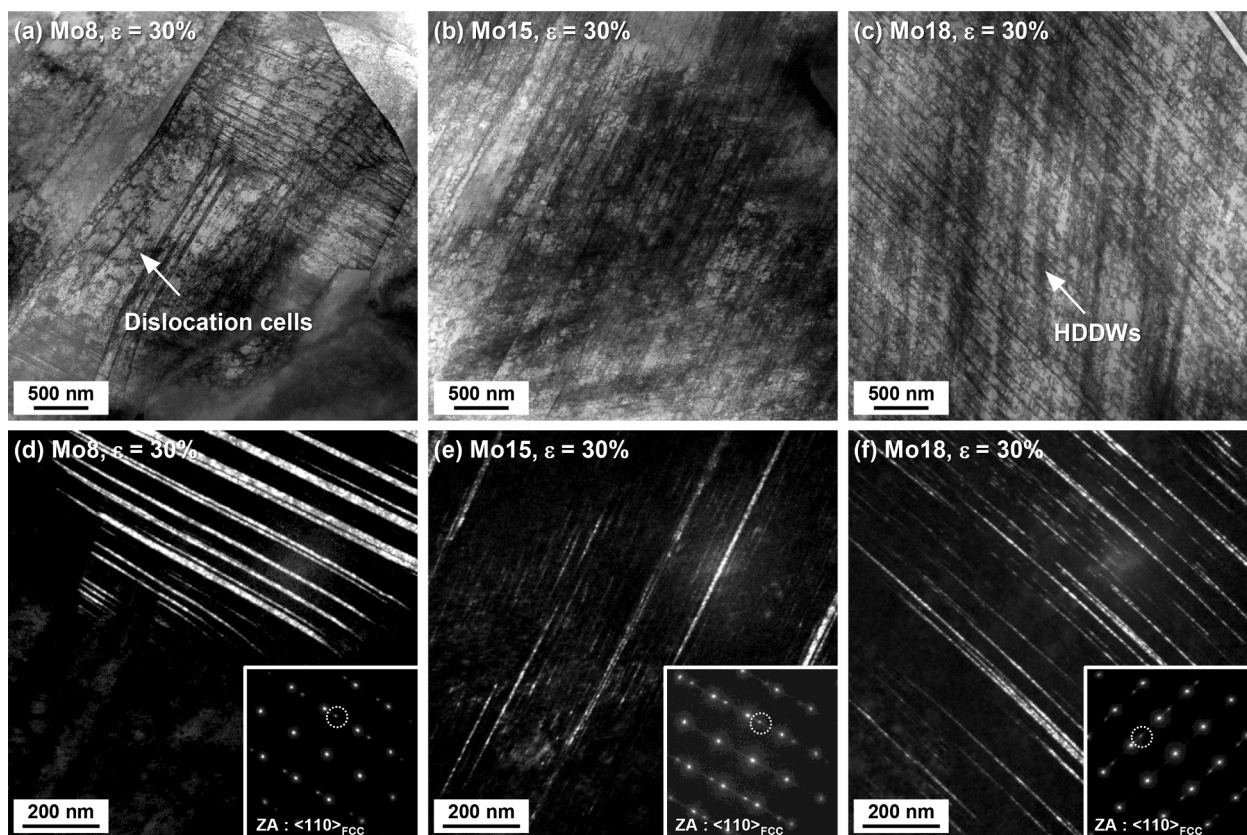

Fig. 8. Deformation structure of the Mo8, Mo15, and Mo18 alloys, with similar grain sizes, deformed to an engineering strain of 30%. STEM images of the (a) Mo8, (b) Mo15, and (c) Mo18 alloys. Corresponding DF images and SADPs (inset) showing the twin substructures of the (d) Mo8, (e) Mo15, and (f) Mo18 alloys.

increase the RMS atomic displacements of the alloys. In particular, when the concentration of Mo reaches 20 at%, the RMS atomic displacement is comparable to that of the VCoNi alloy with high solid-solution strengthening attributed to severe lattice distortion [8]. Consequently,

the above *ab initio* calculations for charge transfer and RMS displacement indicate that Mo plays an effective role in increasing the lattice distortion in the $(CoNi)_{100-x}Mo_x$ system. Additionally, these results indicate that the correlation between lattice distortion and

Table 4

Atomic size difference (δ), atomic packing parameter (γ), mixing enthalpy (ΔH_{mix}), and average valance electron concentration (VEC) of the various FCC CCAs, CoNi binary alloy, and pure Ni.

|	δ (%)	γ	VEC	ΔH_{mix} (kJ mol^{-1})
Ni	-	-	10	-
Ni-40Co	0.0	1.000	9.6	0
FeCoNi	0.75	1.017	9	-1.3
CrCoNi	1.12	1.026	8.3	-4.9
$V_{0.4}Cr_{0.6}CoNi$	2.66	1.087	8.2	-8.8
$V_{0.7}Cr_{0.3}CoNi$	3.26	1.087	8.1	-11.6
VCoNi	3.67	1.087	8	-14.2
CrFeCoNi	1.03	1.026	8.3	-3.8
CrFeMnCoNi	0.92	1.026	8	-4.2
$(CoNi)_{92}Mo_8$	3.22	1.132	9.2	-1.8
$(CoNi)_{85}Mo_{15}$	4.21	1.132	9.0	-3.1
$(CoNi)_{82}Mo_{18}$	4.51	1.132	8.9	-3.5

solid-solution strengthening can be extended to the $(CoNi)_{100-x}Mo_x$ alloys that include the refractory element Mo.

4.2. Grain-boundary strengthening

In addition to solid-solution strengthening from the distorted lattice of the $(CoNi)_{100-x}Mo_x$ alloys, grain-boundary strengthening contributes to their high yield strength. Particularly, in the case of Mo18, which exhibits a yield strength of ~1 GPa, the strengthening contribution of grain-boundary strengthening accounts for ~77% of the total value of

yield strength, indicating a strong sensitivity of the yield strength to grain refinement. To reveal the fundamental mechanism of grain-boundary strengthening represented by the Hall–Petch relation, various models were proposed. Based on the model with a grain-interior source of dislocations (Frank–Read source), the higher friction stress leads to a higher Hall–Petch coefficient [8,74]. It is confirmed that the friction stress, representative of solid-solution strengthening, and the Hall–Petch coefficient are correlated in the $(CoNi)_{100-x}Mo_x$ alloys (Supplementary Fig. 5). However, the linear tendency of the present alloys deviates toward higher Hall–Petch coefficients in comparison with other alloys, implying that only the correlation between solid-solution strengthening and Hall–Petch coefficient is insufficient for unraveling the origin of the strong sensitivity of the yield strength to grain refinement in the $(CoNi)_{100-x}Mo_x$ alloys.

To account for the high Hall–Petch coefficients of the $(CoNi)_{100-x}Mo_x$ alloys, their SFE may be considered. Okamoto et al. [75] described that the reduction of SFE causes the increase of the Hall–Petch coefficient for FCC metals. Thus, to investigate the effect of Mo on SFEs in the $(CoNi)_{100-x}Mo_x$ alloys, SFEs were computed through *ab initio* calculations, as shown in Fig. 10. For the equiatomic CoNi alloy (x=0), the computed SFE is approximately 10 mJ/m^2 at 0 K. This is in reasonable agreement with previously reported *ab initio* SFE [76,77]. With an increase in Mo content, the SFE continuously decreases to negative values. Such negative *ab initio* SFEs at 0 K are often found in various 3d-transition metal-based HEAs [77–79]. Finite-temperature lattice vibrations slightly increase the SFE (Fig. 10c), as also found in a previous study [13], whereas the compositional trend may not be largely affected by
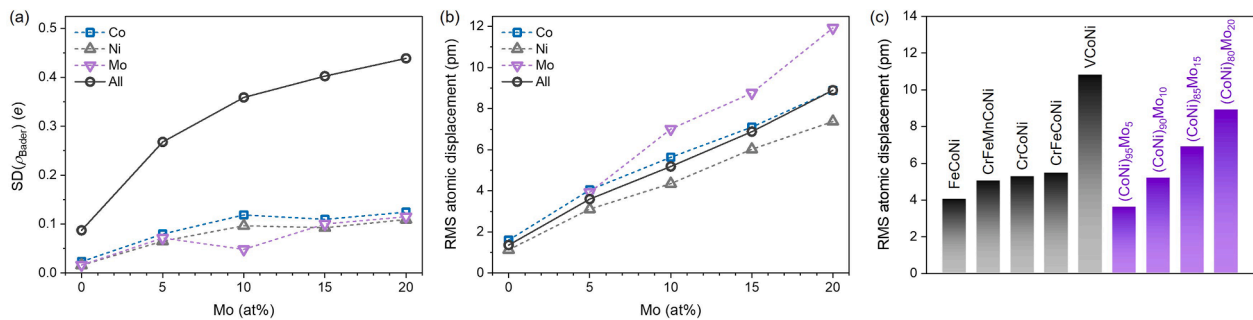
Fig. 9. *Ab initio* calculations for the lattice distortion of the $(CoNi)_{100-x}Mo_x$ system (x = 0–20 at%). (a) Standard deviation (SD) of the Bader charges and (b) RMS displacements of alloys as a function of the Mo content. The solid black lines show the values for all the elements, whereas the dotted blue, gray, and purple lines show the values of Co, Ni, and Mo, respectively. (c) The RMS displacement for various FCC CCAs [8].
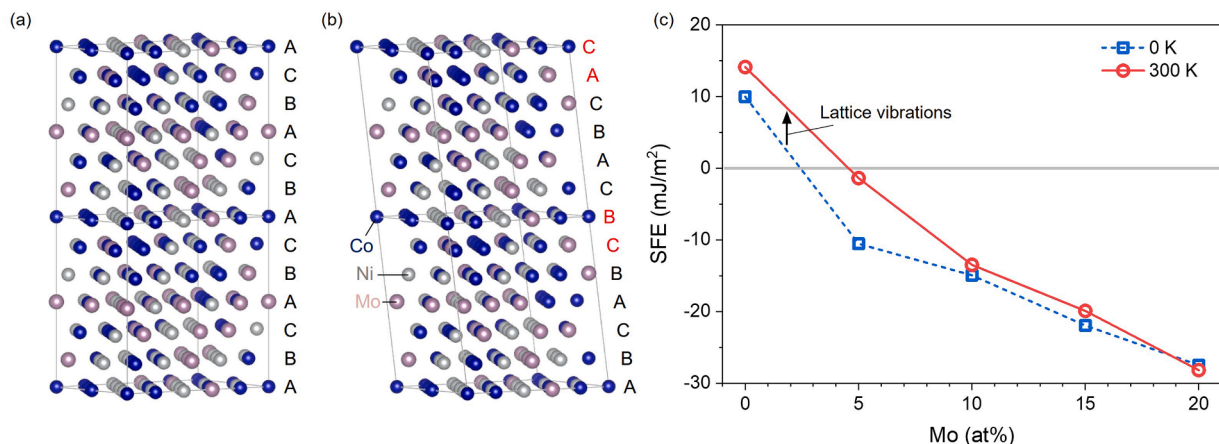
Fig. 10. *Ab initio* calculations for the SFE of the $(CoNi)_{100-x}Mo_x$ system (x = 0–20 at%). Example for supercell models of chemically disordered FCC $(CoNi)_{80}Mo_{20}$ alloy (a) without SFs and (b) with a SF obtained by the tilted-supercell approach. Labels A, B, and C correspond to the stacking sequence of the {111} planes, and the interlayer spaces sandwiched by the red labels to the SFs. The simulation cells are repeated twice along the ⟨111⟩ direction to better visualize the tilted-supercell approach. (c) *Ab initio* SFEs of the alloys as a function of the Mo content. The dashed blue and the solid red lines show the results at 0 K and at 300 K with the contributions of lattice vibrations, respectively.

such finite temperature contributions [80]. Other factors, such as chemical short-range order [81] and interstitial alloying [82] may also modify the SFE.

To verify the characteristic tendency of the SFE according to the Mo content obtained through *ab initio* calculations, experimental quantification was conducted for the $(CoNi)_{100-x}Mo_x$ alloys at room temperature through weak-beam DF TEM analysis (Fig. 11). The SFE of each alloy was calculated based on partial dislocation analysis. The weak-beam DF TEM images acquired from <111> zone axis using three independent <220>-type g vectors for the 2%-strained Mo18 specimen in Fig. 11a–c reveal the extended SF formed by dissociation of a perfect dislocation into two Shockley partial dislocations. The Burgers vectors of the individual dislocations were identified using the g·b = 0 technique. In the DF image using g = 20$\bar{2}$ (Fig. 11a), both partial dislocations are visible, but in the DF images using g = 02$\bar{2}$ (Fig. 11b) and g = 2$\bar{2}$0 (Fig. 11c), one of the two partial dislocations is invisible. The 2%-strained Mo15 and Mo8 specimens were also analyzed via identical Burgers vector analysis as shown in Fig. 11d,e, revealing that the expanded width of dissociated partial dislocations increases from 10.4 nm to 22.0 nm with the increase in Mo content. Consequently, the SFE of the Mo8, Mo15, and Mo18 alloys were estimated as 19.6, 14.6, and 6.4 mJ/m^2, respectively (Fig. 11f). In good agreement with the compositional trend observed in the theoretical prediction, the SFE decreases considerably with increasing Mo content. Additionally, it is notable that the $(CoNi)_{100-x}Mo_x$ alloys present lower SFE values than the CrCoNi alloy (22 mJ/m^2), which is known as a representative FCC CCA with a low SFE [9]. Therefore, both theoretical calculations and experimental measurements demonstrate SFE reduction with increasing Mo content in the $(CoNi)_{100-x}Mo_x$ system. The low SFE values of the $(CoNi)_{100-x}Mo_x$ system can contribute to the enhanced grain-boundary strengthening in terms

of the dislocation multiplication in the lattice. It is generally known that the activation of multiple cross-slip promotes bulk dislocation multiplication through the generation of Frank–Read sources [83]. As discussed in the partial dislocation analysis, the SFE is directly correlated with the interspacing of the dissociated partial dislocations. A low SFE hinders the association of partial dislocations into perfect dislocations, as required for cross-slip. Therefore, the low SFE regime of the current alloys can increase the activation barrier for the multiple cross-slip mechanism and the consequent dislocation multiplication in the grains, resulting in the elevated Hall–Petch coefficient.

However, it should be noted that the Frank–Read source is not the only source of dislocations in polycrystalline materials. Based on the grain-boundary ledge model, at the initiation of plastic deformation, the grain boundary not only hinders the glide of dislocations emitted from the interior source but also acts as a dislocation source itself by dislocation emission from the ledges [84]. In line with this model, the Hall–Petch coefficient is often noted to be affected by grain-boundary segregation. It is reported that the doping of interstitial or substitutional solutes, which results in solute segregation at grain boundaries, can lead to an increase in the Hall–Petch coefficient in ferritic steels [85, 86] and Ni alloys [87]. The grain-boundary segregation can stabilize the dislocation emission site, which makes it harder for the grain boundaries to emit dislocations [88]. Araki et al. [89] demonstrated that the carbon segregation at grain boundaries in ferritic steel increases the critical stress required for dislocation emission. Additionally, molecular dynamics simulations on the quinary CCA revealed that the atomic composition of the grain boundary mediates the stress required for dislocation emission [90]. The increase in the Hall–Petch coefficient through the doping of interstitial solutes has previously been observed even in FCC CCAs [91,92], although the underlying mechanisms have not yet been revealed. In this work, the elemental distribution analysis
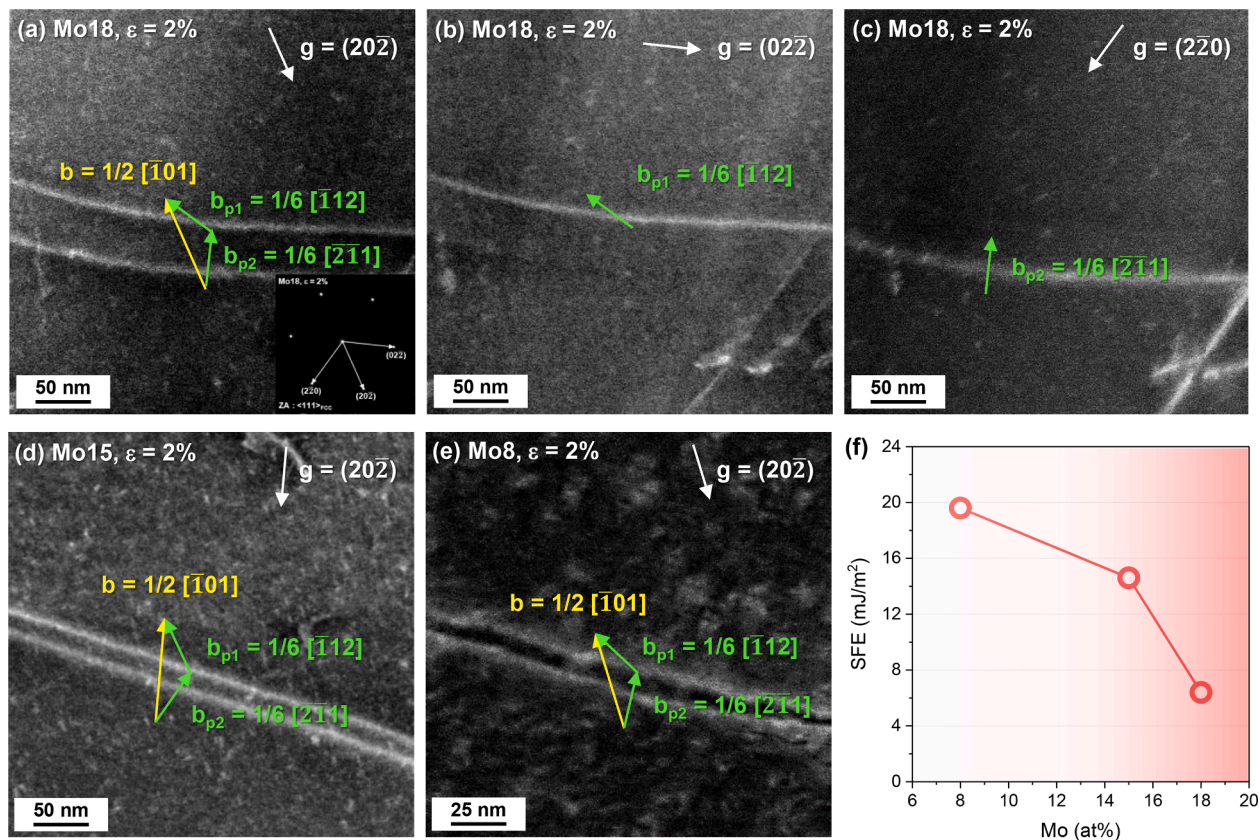
Fig. 11. Dislocation analysis and SFE measurement for the Mo8, Mo15, and Mo18 alloys deformed to an engineering strain of 2%. (a) SADP (inset) obtained from <111> zone axis of the Mo18 specimen and the corresponding weak beam DF TEM images using g = 20$\bar{2}$ (b) g = 02$\bar{2}$, and (c) g = 2$\bar{2}$0. Weak beam DF images of the (d) Mo15 and (e) Mo8 alloys using g = 20$\bar{2}$, where both partial dislocations are visible. (f) Measured SFEs of the alloys as a function of the Mo content.

clearly reveals the presence of enrichment of Mo atoms at the grain boundary by ~10% higher than the matrix (Fig. 5). This result suggests that the unusual Hall–Petch coefficients of the $(CoNi)_{100-x}Mo_x$ alloys originate from the stabilization of grain-boundary sources by employing Mo segregation. In consequence, the specific Hall–Petch coefficients of the $(CoNi)_{100-x}Mo_x$ alloys are influenced by the three factors associated with the addition of Mo element: elevated solid-solution strengthening, reduced SFE, and grain-boundary segregation of Mo element. However, the ongoing debate regarding the dominant dislocation source mechanism in polycrystalline metals [93] makes it challenging to independently differentiate the influence of each factor on the grain-boundary strengthening in the current alloys. Moreover, the degree of segregation may vary with annealing conditions, and other factors such as texture [94], annealing twin density [21], and dislocation arrangement [95] can influence the Hall–Petch coefficient. Thus, more systematic investigations are required to reveal the details of grain-boundary strengthening in the present alloys.

4.3. Deformation mechanisms and strain-hardening capability

The effects of the Mo content on mechanical responses are featured by the enhanced yield strength that stands for the initiation of plastic deformation and also the variations in subsequent strain-hardening behaviors. All the alloys exhibit dislocation glides and SF formation in the initial plastic region (2% strain, Fig. 7), whereas the planar characteristics of the dislocation arrangements are intensified with increasing Mo content. With further straining (30% strain, Fig. 8), where SFs develop into deformation twins, a refinement of the twin substructures and transition of dislocation substructures from DCs to HDDWs are observed with the change in Mo content. Notably, the deformation mechanisms observed in these alloys are associated with low-SFE regimes. It is generally known that SFE is a key parameter governing the deformation mechanisms of FCC-structured materials [96]. As discussed earlier, the reduction of SFE hampers cross-slip, allowing planar slip to be dominant during plastic deformation [97]. In other words, dislocations are typically accumulated in the form of HDDWs (planar slips) rather than DCs (wavy slips). Thus, the increasing Mo content reduces the SFE and results in the transition of the dislocation substructure from DCs (Mo8) to HDDWs (Mo18) (Fig. 8a–c). In addition, the deformation twinning substructure is affected by the SFE in the $(CoNi)_{100-x}Mo_x$ alloys. Because cross-slip plays an important role in the thickening of deformation twins [98], the obstruction of cross-slip due to the elevated Mo content and the reduced SFE suppresses the thickening of deformation twins and thus contributes to the formation of fine twin substructures in Mo15 and Mo18. It has also been demonstrated that the enhanced solid-solution strengthening in FCC CCAs retards cross-slip by imposing higher friction stress on partial dislocations [13].

In terms of strain hardening, a higher Mo content induces higher strain-hardening rates (Fig. 6e) and consequently improves both strength and ductility (Fig. 6f). This tendency can be explained by the variation in the SFE according to the Mo content. The transition of dislocation substructures from DCs to HDDWs enables gliding dislocations to be accumulated more densely inside the grains by impeding cross-slip and the subsequent dynamic recovery during plastic deformation [99]. Moreover, the refinement of twin substructures introduces additional effective interfaces that induce a reduction in the dislocation mean free path, which is referred to as the dynamic Hall–Petch effect [100]. Thus, with increasing Mo content, both contributions significantly hindered dislocation glides and increased the strain-hardening rate, which enabled the alloys to overcome the strength-ductility trade-off. In particular, Mo18 presents an excellent strength–ductility combination of 1326 MPa×51.5%, stemming from its high solid-solution strengthening, grain-boundary strengthening, and strain-hardening capability. Notably, the present investigation, which demonstrated the synergetic effect of Mo on strength and ductility in single FCC structured $(CoNi)_{100-x}Mo_x$ alloys with a broad range of Mo content, suggest the possibility of expanded compositional space in FCC CCAs and thus extended mechanical properties.

5. Conclusions

In this study, the microstructural evolutions and mechanical properties of the $(CoNi)_{100-x}Mo_x$ alloys (Mo8, Mo15, and Mo18) were systematically investigated. The underlying effect of Mo on the phase stability and mechanical properties was investigated via theoretical calculations and experimental measurements, which led to the following conclusions.

(1) A single FCC solid solution was maintained up to 18 at% Mo in the $(CoNi)_{100-x}Mo_x$ system. With increasing Mo content, the minimum temperature required to form a single FCC solid solution increased to 1000°C and 1050°C in the Mo15 and Mo18 alloys, respectively. At lower temperatures, the single FCC solid solution in both alloys decomposed into disordered FCC and HCP solid solutions and ordered $D0_{19}$, whereas the Mo8 alloy remained in the FCC solid solution at 700°C.

(2) For the Mo8, Mo15, and Mo18 alloys with a single FCC solid solution whose grain sizes were tailored to a range of ~2–60 μm, both the strength and the ductility improved simultaneously from Mo8 to Mo18. Particularly, the Mo18 alloy exhibited an outstanding yield strength of ~1 GPa, a tensile strength of ~1.3 GPa, and ductility of ~50%, despite being in the recrystallized single FCC solid-solution state.

(3) Through *ab initio* calculations of the charge transfer and RMS displacement, it was revealed that Mo played an effective role in increasing the lattice distortion in $(CoNi)_{100-x}Mo_x$ systems. The increase in the lattice distortion induced by the introduction of Mo enhanced the solid-solution strengthening from 59 MPa in the CoNi alloy to 229 MPa in the Mo18 alloy. This result indicated that lattice distortion and solid-solution strengthening correlated well even in the $(CoNi)_{100-x}Mo_x$ alloys that include the refractory element Mo.

(4) The $(CoNi)_{100-x}Mo_x$ alloys exhibited a strong sensitivity of yield strength to grain refinement compared to other FCC CCAs composed of 3d-transition metals. The enhanced Hall-Petch coefficients observed in these alloys can be attributed to the synergistic effects of several factors associated with the addition of Mo, such as elevated solid-solution strengthening, reduced SFE, and segregation of Mo at grain boundaries. However, due to the difficulty in distinguishing the individual contributions of these factors, further systematic investigations are required to thoroughly elucidate their roles.

(5) During tensile deformation, the higher Mo content induced a higher strain-hardening rate and consequently improved both strength and ductility. The decreased SFE with elevated Mo content caused the transition of the dislocation substructure from DCs to HDDWs and the refinement of twin substructures. Both transitions in the dislocation and twin substructures significantly hindered dislocation glides and produced a higher strain-hardening capability.

CRediT authorship contribution statement

Tae Jin Jang: Conceptualization, Methodology, Validation, Formal analysis, Investigation, Writing – original draft, Writing – review & editing. **You Na Lee:** Investigation, Methodology, Validation, Writing – review & editing. **Yuji Ikeda:** Supervision, Validation, Writing – review & editing. **Fritz Körmann:** Supervision, Validation, Writing – review & editing. **Ju-Hyun Baek:** Investigation. **Hyeon-Seok Do:** Investigation. **Yeon Taek Choi:** Investigation. **Hojun Gwon:** Investigation. **Jin-Yoo Suh:** Supervision, Validation. **Hyoung Seop Kim:** Supervision, Validation. **Byeong-Joo Lee:** Supervision, Validation. **Alireza Zargaran:**

Investigation, Visualization, Supervision, Validation, Writing – review & editing. **Seok Su Sohn:** Project administration, Conceptualization, Visualization, Supervision, Validation, Writing – review & editing.

Supplementary materials

Supplementary material associated with this article can be found, in the online version, at doi:10.1016/j.actamat.2023.119030.

References

[1] Z.P. Lu, H. Wang, M.W. Chen, I. Baker, J.W. Yeh, C.T. Liu, T.G. Nieh, An assessment on the future development of high-entropy alloys: summary from a recent workshop, Intermetallics 66 (2015) 67–76.

[2] D.B. Miracle, O.N. Senkov, A critical review of high entropy alloys and related concepts, Acta Mater. 122 (2017) 448–511.

[3] E.P. George, D. Raabe, R.O. Ritchie, High-entropy alloys, Nat. Rev. Mater. 4 (2019) 515–534.

[4] Z. Wu, H. Bei, G.M. Pharr, E.P. George, Temperature dependence of the mechanical properties of equiatomic solid solution alloys with face-centered cubic crystal structures, Acta Mater. 81 (2014) 428–441.

[5] B. Gludovatz, A. Hohenwarter, D. Catoor, E.H. Chang, E.P. George, R.O. Ritchie, A fracture-resistant high-entropy alloy for cryogenic applications, Science 345 (2014) 1153–1158.

[6] F.D.C. Garcia Filho, R.O. Ritchie, M.A. Meyers, S.N. Monteiro, Cantor-derived medium-entropy alloys: bridging the gap between traditional metallic and high-entropy alloys, J. Mater. Res. Technol. 17 (2022) 1868–1895.

[7] B. Gludovatz, A. Hohenwarter, K.V.S. Thurston, H. Bei, Z. Wu, E.P. George, R.O. Ritchie, Exceptional damage-tolerance of a medium-entropy alloy CrCoNi at cryogenic temperatures, Nat. Commun. 7 (2016) 10602.

[8] S.S. Sohn, A. Kwiatkowski da Silva, Y. Ikeda, F. Kormann, W. Lu, W.S. Choi, B. Gault, D. Ponge, J. Neugebauer, D. Raabe, Ultrastrong medium-entropy single-phase alloys designed via severe lattice distortion, Adv. Mater. 31 (2019), 1807142.

[9] G. Laplanche, A. Kostka, C. Reinhart, J. Hunfeld, G. Eggeler, E.P. George, Reasons for the superior mechanical properties of medium-entropy CrCoNi compared to high-entropy CrMnFeCoNi, Acta Mater. 128 (2017) 292–303.

[10] Y.L. Zhao, T. Yang, Y. Tong, J. Wang, J.H. Luan, Z.B. Jiao, D. Chen, Y. Yang, A. Hu, C.T. Liu, J.J. Kai, Heterogeneous precipitation behavior and stacking-fault-mediated deformation in a CoCrNi-based medium-entropy alloy, Acta Mater. 138 (2017) 72–82.

[11] Z. Li, K.G. Pradeep, Y. Deng, D. Raabe, C.C. Tasan, Metastable high-entropy dual-phase alloys overcome the strength–ductility trade-off, Nature 534 (2016) 227–230.

[12] D.G. Kim, Y.H. Jo, J. Yang, W.M. Choi, H.S. Kim, B.J. Lee, S.S. Sohn, S. Lee, Ultrastrong duplex high-entropy alloy with 2 GPa cryogenic strength enabled by an accelerated martensitic transformation, Scr. Mater. 171 (2019) 67–72.

[13] H. Chung, D.W. Kim, W.J. Cho, H.N. Han, Y. Ikeda, S. Ishibashi, F. Kormann, S.S. Sohn, Effect of solid-solution strengthening on deformation mechanisms and strain hardening in medium-entropy $V_{1-x}Cr_xCoNi$ alloys, J. Mater. Sci. Technol. 108 (2022) 270–280.

[14] Y. Zhang, Y.J. Zhou, J.P. Lin, G.L. Chen, P.K. Liaw, Solid-solution phase formation rules for multi-component alloys, Adv. Eng. Mater. 10 (2008) 534–538.

[15] S. Yang, J. Lu, F. Xing, L. Zhang, Y. Zhong, Revisit the VEC rule in high entropy alloys (HEAs) with high-throughput CALPHAD approach and its applications for material design-A case study with Al–Co–Cr–Fe–Ni system, Acta Mater. 192 (2020) 11–19.

[16] S. Guo, C. Ng, J. Lu, C.T. Liu, Effect of valence electron concentration on stability of fcc or bcc phase in high entropy alloys, J. Appl. Phys. 109 (2011).

[17] S. Yoshida, T. Ikeuchi, T. Bhattacharjee, Y. Bai, A. Shibata, N. Tsuji, Effect of elemental combination on friction stress and Hall-Petch relationship in face-centered cubic high /medium entropy alloys, Acta Mater. 171 (2019) 201–215.

[18] N.L. Okamoto, K. Yuge, K. Tanaka, H. Inui, E.P. George, Atomic displacement in the CrMnFeCoNi high-entropy alloy – a scaling factor to predict solid solution strengthening, AIP Adv. 6 (2016), 125008.

[19] H.S. Oh, S.J. Kim, K. Odbadrakh, W.H. Ryu, K.N. Yoon, S. Mu, F. Kormann, Y. Ikeda, C.C. Tasan, D. Raabe, T. Egami, E.S. Park, Engineering atomic-level complexity in high-entropy and complex concentrated alloys, Nat. Commun. 10 (2019) 2090.

[20] H.S. Oh, K. Odbadrakh, Y. Ikeda, S. Mu, F. Kormann, C.J. Sun, H.S. Ahn, K.N. Yoon, D. Ma, C.C. Tasan, T. Egami, E.S. Park, Element-resolved local lattice distortion in complex concentrated alloys: an observable signature of electronic effects, Acta Mater. 216 (2021), 117135.

[21] M. Schneider, E.P. George, T.J. Manescau, T. Záležák, J. Hunfeld, A. Dlouhý, G. Eggeler, G. Laplanche, Analysis of strengthening due to grain boundaries and annealing twin boundaries in the CrCoNi medium-entropy alloy, Int. J. Plast. 124 (2020) 155–169.

[22] M. Schneider, F. Werner, D. Langenkämper, C. Reinhart, G. Laplanche, Effect of temperature and texture on hall–petch strengthening by grain and annealing twin boundaries in the MnFeNi medium-entropy alloy, Metals 9 (2019) 84.

[23] T.J. Jang, W.S. Choi, D.W. Kim, G. Choi, H. Jun, A. Ferrari, F. Kormann, P.P. Choi, S.S. Sohn, Shear band-driven precipitate dispersion for ultrastrong ductile medium-entropy alloys, Nat. Commun. 12 (2021) 4703.

[24] L. Xia, Q. Wu, K. Zhou, B. Han, F. He, Z. Wang, Concurrent recrystallization and precipitation for combination of superior precipitation and grain boundary hardening in $Co_{37}Cr_{20}Ni_{37}Ti_3Al_3$ high-entropy alloy, Met. Mater. Int. 28 (2022) 2863–2879.

[25] W.H. Liu, Z.P. Lu, J.Y. He, J.H. Luan, Z.J. Wang, B. Liu, Y. Liu, M.W. Chen, C.T. Liu, Ductile CoCrFeNiMo$_x$ high entropy alloys strengthened by hard intermetallic phases, Acta Mater. 116 (2016) 332–342.

[26] K. Ming, X. Bi, J. Wang, Precipitation strengthening of ductile $Cr_{15}Fe_{20}Co_{35}Ni_{20}Mo_{10}$ alloys, Scr. Mater. 137 (2017) 88–93.

[27] Park, H.D., Won, J.W., Moon, J., Kim, H.S., Sung, H., Seol, J.B., Bae, J.W., Kim, J.G. Fe55Co17.5Ni10Cr12.5Mo5 high-entropy alloy with outstanding cryogenic mechanical properties driven by deformation-induced phase transformation behavior, Met. Mater. Int. 29 (2023) 95–107.

[28] N. Li, J. Gu, B. Gan, Q. Qiao, S. Ni, M. Song, Effect of Mo-doping on the microstructure and mechanical properties of CoCrNi medium entropy alloy, J. Mater. Res. 35 (2020) 2726–2736.

[29] Chang, R., Fang, W., Yu, H., Bai, X., Zhang, X., Liu, B., Yin, F. Heterogeneous banded precipitation of (CoCrNi)93Mo7 medium entropy alloys towards strength–ductility synergy utilizing compositional inhomogeneity, Scr. Mater. 172 (2019) 144–148.

[30] R. Chang, W. Fang, J. Yan, H. Yu, X. Bai, J. Li, S. Wang, S. Zheng, F. Yin, Microstructure and mechanical properties of CoCrNi-Mo medium entropy alloys: experiments and first-principle calculations, J. Mater. Sci. Technol. 62 (2021) 25–33.

[31] Z. Cheng, W. Zhu, L. Yang, C. Zhao, P. Wei, F. Ren, Tuning the mechanical properties of Fe$_x$(CoMoNi)$_{100-x}$ high-entropy alloys via controlled formation of hard μ phase, Mater. Sci. Eng. A 773 (2020), 138881.

[32] J. He, S.K. Makineni, W. Lu, Y. Shang, Z. Lu, Z. Li, B. Gault, On the formation of hierarchical microstructure in a Mo-doped NiCoCr medium-entropy alloy with enhanced strength-ductility synergy, Scr. Mater. 175 (2020) 1–6.

[33] D.J.H. Cockayne, A theoretical analysis of the weak-beam method of electron microscopy, Z. Naturforsch. A 27 (1972) 452–460.

[34] H.J. Kim, M.K. Cho, G. Kim, S.Y. Lee, M.G. Jo, H. Kim, J.Y. Suh, J. Lee, Influence of hydrogen absorption on stacking fault of energy of a face-centered cubic high entropy alloy, Met. Mater. Int. 28 (2022) 2637–2645.

[35] A. Zunger, S.H. Wei, L.G. Ferreira, J.E. Bernard, Special quasirandom structures, Phys. Rev. Lett. 65 (1990) 353–356.

[36] M. Ångqvist, W.A. Muñoz, J.M. Rahm, E. Fransson, C. Durniak, P. Rozyczko, T.H. Rod, P. Erhart, ICET – a python library for constructing and sampling alloy cluster expansions, Adv. Theory Simul. 2 (2019), 1900015.

[37] H. Gholizadeh, C. Draxl, P. Puschnig, The influence of interstitial carbon on the γ-surface in austenite, Acta Mater. 61 (2013) 341–349.

[38] X. Zhang, B. Grabowski, F. Körmann, A.V. Ruban, Y. Gong, R.C. Reed, T. Hickel, J. Neugebauer, Temperature dependence of the stacking-fault Gibbs energy for Al, Cu, and Ni, Phys. Rev. B 98 (2018), 224106.

[39] Ikeda, Y., Körmann, F., Tanaka, I., Neugebauer, J. Impact of chemical fluctuations on stacking fault energies of CrCoNi and CrMnFeCoNi high entropy alloys from first principles, Entropy, 20 (2018) 655.

[40] S. Zhao, Y. Osetsky, G.M. Stocks, Y. Zhang, Local-environment dependence of stacking fault energies in concentrated solid-solution alloys, NPJ Comput. Mater. 5 (2019) 13.

[41] G. Kresse, Ab initio molecular dynamics for liquid metals, J. Non-Cryst. Solids 192-193 (1995) 222–229.

[42] G. Kresse, J. Furthmüller, Efficiency of ab-initio total energy calculations for metals and semiconductors using a plane-wave basis set, Comput. Mater. Sci. 6 (1996) 15–50.

[43] G. Kresse, D. Joubert, From ultrasoft pseudopotentials to the projector augmented-wave method, Phys. Rev. B 59 (1999) 1758–1775.

[44] P.E. Blöchl, Projector augmented-wave method, Phys. Rev. B 50 (1994) 17953–17979.

[45] J.P. Perdew, K. Burke, M. Ernzerhof, Generalized gradient approximation made simple, Phys. Rev. Lett. 77 (1996) 3865–3868.

[46] M. Methfessel, A.T. Paxton, High-precision sampling for Brillouin-zone integration in metals, Phys. Rev. B 40 (1989) 3616–3621.

[47] P. Vinet, J.R. Smith, J. Ferrante, J.H. Rose, Temperature effects on the universal equation of state of solids, Phys. Rev. B 35 (1987) 1945–1953.

[48] A. Otero-de-la-Roza, V. Luaña, Gibbs2: a new version of the quasi-harmonic model code. I. Robust treatment of the static data, Comput. Phys. Commun. 182 (2011) 1708–1720.

[49] A. Otero-de-la-Roza, D. Abbasi-Pérez, V. Luaña, Gibbs2: a new version of the quasiharmonic model code. II. Models for solid-state thermodynamics, features and implementation, Comput. Phys. Commun. 182 (2011) 2232–2248.

[50] M. Yu, D.R. Trinkle, Accurate and efficient algorithm for Bader charge integration, J. Chem. Phys. 134 (2011), 064111.

[51] G. Henkelman, A. Arnaldsson, H. Jónsson, A fast and robust algorithm for Bader decomposition of charge density, Comput. Mater. Sci. 36 (2006) 354–360.

[52] E. Sanville, S.D. Kenny, R. Smith, G. Henkelman, Improved grid-based algorithm for Bader charge allocation, J. Comput. Chem. 28 (2007) 899–908.

[53] W. Tang, E. Sanville, G. Henkelman, A grid-based Bader analysis algorithm without lattice bias, J. Phys. Condens. Matter 21 (2009), 084204.

[54] W.M. Choi, Y.H. Jo, D.G. Kim, S.S. Sohn, S. Lee, B.J. Lee, A thermodynamic description of the Co-Cr-Fe-Ni-V system for high-entropy alloy design, Calphad 66 (2019), 101624.

[55] H.S. Do, W.M. Choi, B.J. Lee, A thermodynamic description for the Co–Cr–Fe–Mn–Ni system, J. Mater. Sci. 57 (2022) 1373–1389.

[56] Lee, B.J., Sundman, B. TCFE2000: *The Thermo-Calc Steels Database KTH* (KTH, Stockholm, 1999).

[57] Wu, Z. Temperature and alloying effects on the mechanical properties of equiatomic FCC solid solution alloys. PhD diss., University of Tennessee (2014).

[58] Z. Nishiyama, Martensitic Transformation, Elsevier, 2012.

[59] P. Carvalho, B.J. Kooi, J.T.M. De Hosson, Identification of planar defects in D0$_{19}$ phases using high-resolution transmission electron microscopy, Philos. Mag. Lett. 81 (2001) 697–707.

[60] L. Li, Z. Li, A. Kwiatkowski da Silva, Z. Peng, H. Zhao, B. Gault, D. Raabe, Segregation-driven grain boundary spinodal decomposition as a pathway for phase nucleation in a high-entropy alloy, Acta Mater. 178 (2019) 1–9.

[61] E.O. Hall, The deformation and ageing of mild steel: III discussion of results, Proc. Phys. Soc. Sect. B 64 (9) (1951) 747–753.

[62] N.J. Petch, The cleavage strength of polycrystals, J. Iron Steel Inst. 174 (1953) 25–28.

[63] C.Y. Yu, P.W. Kao, C.P. Chang, Transition of tensile deformation behaviors in ultrafine-grained aluminum, Acta Mater. 53 (2005) 4019–4028.

[64] H. Biermann, C.G. Aneziris, Austenitic TRIP/TWIP Steels and Steel-Zirconia Composites: Design of Tough, Transformation-Strengthened Composites and Structures, Springer, 2020.

[65] E. Welsch, D. Ponge, S.M. Hafez Haghighat, S. Sandlöbes, P.P. Choi, M. Herbig, S. Zaefferer, D. Raabe, Strain hardening by dynamic slip band refinement in a high-Mn lightweight steel, Acta Mater. 116 (2016) 188–199.

[66] P.M. Anderson, J.P. Hirth, J. Lothe, Theory of Dislocations, Cambridge University Press, 2017.

[67] Z. Wang, Y. Huang, Y. Yang, J. Wang, C.T. Liu, Atomic-size effect and solid solubility of multicomponent alloys, Scr. Mater. 94 (2015) 28–31.

[68] C. Kittel, P. McEuen, P. McEuen, Introduction to Solid State Physics, Wiley, New York, 1996.

[69] Y. Zhang, T.T. Zuo, Z. Tang, M.C. Gao, K.A. Dahmen, P.K. Liaw, Z.P. Lu, Microstructures and properties of high-entropy alloys, Prog. Mater. Sci. 61 (2014) 1–93.

[70] Y.Y. Zhao, T.G. Nieh, Correlation between lattice distortion and friction stress in Ni-based equiatomic alloys, Intermetallics 86 (2017) 45–50.

[71] C. Varvenne, A. Luque, W.A. Curtin, Theory of strengthening in fcc high entropy alloys, Acta Mater. 118 (2016) 164–176.

[72] S. Ishibashi, Y. Ikeda, F. Körmann, B. Grabowski, J. Neugebauer, Correlation analysis of strongly fluctuating atomic volumes, charges, and stresses in body-centered cubic refractory high-entropy alloys, Phys. Rev. Mater. 4 (2020), 023608.

[73] T. Kostiuchenko, A.V. Ruban, J. Neugebauer, A. Shapeev, F. Körmann, Short-range order in face-centered cubic VCoNi alloys, Phys. Rev. Mater. 4 (2020), 113802.

[74] R. Armstrong, I. Codd, R.M. Douthwaite, N.J. Petch, The plastic deformation of polycrystalline aggregates, Philos. Mag. 7 (1962) 45–58.

[75] N.L. Okamoto, S. Fujimoto, Y. Kambara, M. Kawamura, Z.M.T. Chen, H. Matsunoshita, K. Tanaka, H. Inui, E.P. George, Size effect, critical resolved

[76] M. Chandran, S.K. Sondhi, First-principle calculation of stacking fault energies in Ni and Ni-Co alloy, J. Appl. Phys. 109 (2011), 103525.

[77] S. Zhao, G.M. Stocks, Y. Zhang, Stacking fault energies of face-centered cubic concentrated solid solution alloys, Acta Mater. 134 (2017) 334–345.

[78] Z. Zhang, H. Sheng, Z. Wang, B. Gludovatz, Z. Zhang, E.P. George, Q. Yu, S.X. Mao, R.O. Ritchie, Dislocation mechanisms and 3D twin architectures generate exceptional strength-ductility-toughness combination in CrCoNi medium-entropy alloy, Nat. Commun. 8 (2017) 14390.

[79] Y.H. Zhang, Y. Zhuang, A. Hu, J.J. Kai, C.T. Liu, The origin of negative stacking fault energies and nano-twin formation in face-centered cubic high entropy alloys, Scr. Mater. 130 (2017) 96–99.

[80] Z. Li, F. Körmann, B. Grabowski, J. Neugebauer, D. Raabe, Ab initio assisted design of quinary dual-phase high-entropy alloys with transformation-induced plasticity, Acta Mater. 136 (2017) 262–270.

[81] J. Ding, Q. Yu, M. Asta, R.O. Ritchie, Tunable stacking fault energies by tailoring local chemical order in CrCoNi medium-entropy alloys, Proc. Natl. Acad. Sci. 115 (2018) 8919–8924.

[82] Y. Ikeda, I. Tanaka, J. Neugebauer, F. Körmann, Impact of interstitial C on phase stability and stacking-fault energy of the CrMnFeCoNi high-entropy alloy, Phys. Rev. Mater. 3 (2019), 113603.

[83] G.E. Dieter, Mechanical Metallurgy, McGraw-Hill, New York, 1998.

[84] V. Bata, E.V. Pereloma, An alternative physical explanation of the Hall–Petch relation, Acta Mater. 52 (2004) 657–665.

[85] F. Jiang, T. Masumura, T. Tsuchiyama, S. Takaki, Effect of substitutional element addition on Hall-Petch relationship in interstitial free ferritic steels, ISIJ Int. 59 (2019) 1929–1931.

[86] S. Araki, K. Fujii, D. Akama, T. Tsuchiyama, S. Takaki, T. Ohmura, J. Takahashi, Effect of low temperature aging on Hall-Petch coefficient in ferritic steels containing a small amount of carbon and nitrogen, ISIJ Int. 58 (2018) 1920–1926.

[87] S. Floreen, J.H. Westbrook, Grain boundary segregation and the grain size dependence of strength of nickel-sulfur alloys, Acta Metall. 17 (1969) 1175–1181.

[88] S. Takaki, D. Akama, N. Nakada, T. Tsuchiyama, Effect of grain boundary segregation of interstitial elements on Hall-Petch coefficient in steels, Mater. Trans. 55 (2014) 28–34.

[89] S. Araki, K. Mashima, T. Masumura, T. Tsuchiyama, S. Takaki, T. Ohmura, Effect of grain boundary segregation of carbon on critical grain boundary strength of ferritic steel, Scr. Mater. 169 (2019) 38–41.

[90] K. Shiotani, T. Niiyama, T. Shimokawa, Dislocation emission from grain boundaries in high-entropy alloys: influenece of atomic composition at grain boundaries, Mater. Trans. 61 (2020) 1272–1279.

[91] I. Moravcik, H. Hadraba, L. Li, I. Dlouhy, D. Raabe, Z. Li, Yield strength increase of a CoCrNi medium entropy alloy by interstitial nitrogen doping at maintained ductility, Scr. Mater. 178 (2020) 391–397.

[92] N.D. Stepanov, D.G. Shaysultanov, R.S. Chernichenko, N.Y. Yurchenko, S.V. Zherebtsov, M.A. Tikhonovsky, G.A. Salishchev, Effect of thermomechanical processing on microstructure and mechanical properties of the carbon-containing CoCrFeNiMn high entropy alloy, J. Alloy. Compd. 693 (2017) 394–405.

[93] L.E. Murr, Dislocation ledge sources: dispelling the myth of Frank–Read source importance, Metall. Mater. Trans. A 47 (2016) 5811–5826.

[94] Y. Wang, H. Choo, Influence of texture on Hall–Petch relationships in an Mg alloy, Acta Mater. 81 (2014) 83–97.

[95] M. Nyström, U. Lindstedt, B. Karlsson, J.O. Nilsson, Influence of nitrogen and grain size on deformation behaviour of austenitic stainless steels, Mater. Sci. Technol. 13 (1997) 560–567.

[96] T.W. Zhang, S.G. Ma, D. Zhao, Y.C. Wu, Y. Zhang, Z.H. Wang, J.W. Qiao, Simultaneous enhancement of strength and ductility in a NiCoCrFe high-entropy alloy upon dynamic tension: micromechanism and constitutive modeling, Int. J. Plast. 124 (2020) 226–246.

[97] D.A. Hughes, Microstructural evolution in a non-cell forming metal: Al–Mg, Acta Metall. Mater. 41 (1993) 1421–1430.

[98] J. Narayan, Y.T. Zhu, Self-thickening, cross-slip deformation twinning model, Appl. Phys. Lett. 92 (2008) 151908.

[99] A. Rohatgi, K.S. Vecchio, G.T. Gray, The influence of stacking fault energy on the mechanical behavior of Cu and Cu-Al alloys: deformation twinning, work hardening, and dynamic recovery, Metall. Mater. Trans. A 32 (2001) 135–145.

[100] I. Gutierrez-Urrutia, D. Raabe, Dislocation and twin substructure evolution during strain hardening of an Fe–22wt.% Mn–0.6wt.% C TWIP steel observed by electron channeling contrast imaging, Acta Mater. 59 (2011) 6449–6462.